ITERATION BASED TEMPORAL SUBCYCLING FINITE-DIFFERENCE TIME-DOMAIN ALGORITHM WITH APPLICATIONS TO THE THROUGH-THE-WALL RADAR DETECTION ANALYSIS

by

PENGLONG XU

A DISSERTATION

Submitted in partial fulfillment of the requirements
for the degree of Doctor of Philosophy in the
Applied Mathematics Program
of Delaware State University

DOVER, DELAWARE
August 2017

This thesis is approved by the following members of the Final Oral Review Committee:

Dr. Jinjie Liu, Committee Chairperson, Department of Mathematical Sciences, Delaware State University
Dr. Matthew Tanzy, Committee Member, Department of Mathematical Sciences, Delaware State University
Dr. Fengshan Liu, Committee Member, Department of Mathematical Sciences, Delaware State University
Dr. Aristides Marcano, Committee Member, Department of Physics and Engineering, Delaware State University
Dr. Moysey Brio, External Committee Member, Department of Mathematics, The University of Arizona

DEDICATION

Dedicated to my family for their love, endless support and encouragement.
I give special thanks to my loving parents and my wife who never left my side and have been believing in me throughout the process. And I would also like to thank all of my friends and colleagues for always being there for me.

ACKNOWLEDGEMENTS

I would like to express my deepest and sincere gratitude to my advisor, Dr. Jinjie Liu, for his excellent guidance, caring, patience, and providing me with an excellent atmosphere for doing research. His wide knowledge and deep insights have been of great value for me in my graduate studies. This research could not have been completed without his care, support and valuable advice.

I would like to thank Dr. Moysey Brio from the University of Arizona and my coadvisor Dr. Fengshan Liu for guiding my research for the past several years. I wish to thank them for their understanding, encouraging and personal guidance which have provided a good basis for the research. I heartily thank other members of my dissertation defense committee Dr. Aristides Marcano and Dr. Matthew Tanzy, who generously give constructive comments and warm encouragement to better my work.

I would also like to acknowledge the AFOSR Grant FA9550-16-1-0199, the US ARO Grant W911NF-11-2-0046 and the NSF Grant HRD-1242067 for their support. I am also thank the Department of Mathematical Science, College of Mathematics, Natural Sciences and Technology and Delaware State University for providing me with the opportunity, resource and the scholarships that made this research possible.

Last but not least, I would like to thank my parents and my wife without their support this thesis would not have been possible.

Iteration Based Temporal Subcycling Finite-Difference Time-Domain Algorithm with Applications to the Through-The-Wall Radar Detection Analysis

Penglong Xu

Faculty Advisor: Dr. Jinjie Liu

ABSTRACT

The finite-difference time-domain (FDTD) method is a widely used numerical technique for solving the time domain Maxwell's equations of electrodynamics. To accurately model small structures in relatively large computational domain, the subgridding technique is applied to save computational cost. In this dissertation, we first investigate the stability of the subgridding FDTD method and show the late-time instability due to temporal subcycling. To overcome the late-time instability problem, we propose a novel stable iteration based temporal subcycling FDTD algorithm for solving the Maxwell's equations in time domain. The stability of our method is analyzed using eigenvalue test and verified by performing long time simulation of millions of steps. Through-the-wall radar imaging (TWRI) is emerging as a viable technology for providing high quality image of enclosed structures. In our research, we apply the proposed temporal subcycling FDTD algorithm to simulate the through-the-wall radar (TWR) and employ a radar imaging method to reconstruct the object.

TABLE OF CONTENTS

LIST OF TABLES . . . . **vii**
LIST OF FIGURES . . . . **viii**
ABBREVIATIONS . . . . **xi**
CHAPTER 1 INTRODUCTION **1**
CHAPTER 2 THE FINITE-DIFFERENCE TIME-DOMAIN METHOD AND SUBGRIDDING TECHNIQUES **6**
2.1 Finite-Difference Time-Domain Method 6
2.2 Perfectly Matched Layer Boundary Condition 7
2.3 Spatial Subgridding 8
2.3.1 The spatial subgridding algorithm with GHC 8
2.3.2 The spatial subgridding algorithm with GHF 12
2.4 Temporal Subcycling 15
2.4.1 The temporal subcycling algorithm with GH 15
2.4.2 The temporal subcycling algorithm with GE 19
CHAPTER 3 THE ITERATION BASED TEMPORAL SUBCYCLING FDTD METHOD **23**
3.1 Iteration Based Temporal Subcycling FDTD Method 23
3.2 Iteration Based Temporal Subcycling and Spatial Subgridding FDTD Method 26
CHAPTER 4 THROUGH-THE-WALL RADAR DETECTION ANALYSIS 31
4.1 Radar Basic Model 31
4.2 Radar Imaging Method 34
4.2.1 Target location detection 34
4.2.2 Target characterization analysis 36
CHAPTER 5 NUMERICAL EXAMPLES **39**
5.1 Numerical Examples for Spatial Subgridding Method 39
5.2 Numerical Examples for Temporal Subcycling Method 42
5.3 Numerical Examples for Iteration Based Subgrrding Algorithm 43
5.4 Numerical Simulations of Through-the-Wall Radar Imaging 46
CHAPTER 6 CONCLUSIONS **57**
REFERENCES **58**

LIST OF TABLES

5.1 List of the maximum eigenvalue for different coarse grid sizes and different subgridding methods. 45

5.2 Convergence test of the iteration based temporal subcycling FDTD algorithm. 45

5.3 The max-eigenvalue for different coarse grid sizes and different temporal subcycling methods. 49

5.4 List of the maximum eigenvalue for different grid sizes by using IBS FDTD method. 49

5.5 The computational error of the results using standard and IBS FDTD methods. 49

LIST OF FIGURES

1.1 A two-dimensional subgridding mesh with separated spatial and temporal coarse/fine mesh interfaces. 4

2.1 A two-dimensional spatial subgridding mesh with spatial coarse/fine mesh ratio 2:1. 9

2.2 The spatial subgridding with GHC for TE_z mode. Blue triangles denote boundary values of the magnetic ghost values. 11

2.3 The spatial subgridding with GHF for TE_z mode. Blue triangles denote boundary values of the magnetic ghost values. 14

2.4 A two-dimensional temporal subcycling mesh with temporal coarse/fine mesh ratio 2:1. 16

2.5 The temporal subcycling with GH for TE_z mode. Blue triangles denote the magnetic ghost values on the fine mesh boundary. 18

2.6 The temporal subcycling with GE for TE_z mode. Blue triangles denote the electric ghost values on the fine mesh boundary. 21

3.1 Flowchart of (a) conventional and (b) iteration based temporal subcycling FDTD method. 24

4.1 Basic principle of the through-the-wall radar. 31

4.2 Signal delay of the through-the-wall radar. 34

4.3 Illustration of the TWR procedure for multiple transmitters and receivers. 35

5.1 The magnetic field (H_{zc}) distribution using (a) the standard FDTD method; (b) the subgridding FDTD with ghost magnetic fields in the coarse region (GHC); and (c) the subgridding FDTD with ghost magnetic fields in the fine region (GHF). The square boxes indicates the boundary of the fine mesh region. 40

5.2 Time history of the magnetic field (H_{zc}) using the (a) GHC, and (b) GHF methods for 1 million time steps. 41

5.3 (a) Distribution of the eigenvalues on the complex plane for the GHC method. (b) Zoom-in view of a region where some eigenvalues fall outside of the unit circle, $|\lambda| > 1$. 42

5.4 Distribution of the eigenvalues on the complex plane for the GHF method. All eigenvalues lie on or inside the unit circle. 43

5.5 The figures show the magnetic field (H_{zc}) distribution using (a) the H ghost value (GH); (b) the E ghost value (GE); and (c) the iteration based temporal subcycling methods. The square box shows the boundary of the fine mesh region. 44

5.6 Distribution of the eigenvalues on the complex plane for the GH subgridding method. All eigenvalues lie on or inside the unit circle. 46

5.7 (a) Distribution of the eigenvalues on the complex plane for the GE subgridding method. (b) Enlarged small region with some eigenvalues outside of the unit circle. 47

5.8 Distribution of the eigenvalues on the complex plane for the iteration based temporal subcycling method. All eigenvalues lie on or inside the unit circle. 48

5.9 The magnetic field (H_{zc}) distribution using the (a) standard and (b) IBS FDTD methods. The square box is the boundary of fine region B. 50

5.10 Time history of the magnetic field (H_{zc}) using the iteration based subgridding FDTD method for 1 million time steps. 50

5.11 Distribution of the eigenvalues on the complex plane for the iteration based subgridding FDTD method. 51

5.12 TWR object reconstruction. All of the ellipses constructed from the transmitters and receivers are shown in this figure. The set of ellipses encircles the object. 51

5.13 Ellipses reconstructed from all of the transmitters and receivers on the (a) left, (b) right, (c) top, and (d) bottom sides. The square outlined in black is the walls of the room and the circle outlined in green is the circular object. The blue points in each images are the transmitters and receivers. 52

5.14 Reconstructed circular objects using (a) the standard FDTD (black circle) and (b) the IBS-FDTD method (red circles). The square outlined in black color is the walls of the room and the circle outlined in green is the actual object. (b) enlarged image. 53

5.15 Reconstructed squared objects using (a) the standard FDTD (black circle) and (b) the IBS-FDTD method (red circles). The square outlined in black color is the walls of the room and the object outlined in green is the actual object. (b) enlarged image. 53

5.16 Reconstruction of circular object (not centered at the room) using (a) one transmitter and (b) multiple transmitters. The square outlined in black is the walls of the room and the circle outlined in green is the actual circular object. 54

5.17 Reconstruction of squared object (not centered at the room) using (a) one transmitter and (b) multiple transmitters. The square outlined in black is the walls of the room and the circle outlined in green is the actual squared object. 54

5.18 Reconstruction of triangular object using (a) one transmitter and (b) multiple transmitters. The square outlined in black is the walls of the room and the triangular outlined in green is the actual triangular object. 55

5.19 Reconstruction of a larger triangular object using (a) one transmitter and (b) multiple transmitters. The square outlined in black is the walls of the room and the triangular outlined in green is the actual triangular object. . 55

5.20 Reconstruction of oblique triangular object (not centered at the room) using (a) one transmitter and (b) multiple transmitters. The square outlined in black is the walls of the room and the oblique triangular outlined in green is the actual oblique triangular object. 56

5.21 Reconstruction of rhombus object (not centered at the room) using (a) one transmitter and (b) multiple transmitters. The square outlined in black is the walls of the room and the rhombus outlined in green is the actual rhombus object. 56

LIST OF ABBREVIATIONS

2D	-	Two Dimensional
3D	-	Three Dimensional
AMR	-	Adaptive Mesh Refinement
CFL	-	Courant-Friedrichs-Lewy
FDTD	-	Finite-Difference Time-Domain
GPR	-	Ground Penetrating Radar
HSG	-	Huygens Subgridding
IBS	-	Iteration Based Subgridding
ITS	-	Iteration Based Temporal Subcycling
PML	-	Perfectly Matched Layer
TWRI	-	Through-The-Wall Radar Imaging
TWR	-	Through-The-Wall Radar
UWB	-	Ultra Wide Band

Chapter 1
INTRODUCTION

Maxwell's equations are a set of partial differential equations governing the propagation of the electromagnetic waves, representing the relationship between the electric field and the magnetic field [23]. This set of differential equations is considered as one of the most important contributions in the history of science. Maxwell's equations have been applied in diverse fields such as geology, biology, optics, medical treatment and others. In geology, the Ground Penetrating Radar (GPR) and Through-the-Wall Radar (TWR) are good candidates among many applications of Maxwell's equations[4, 6, 9, 18, 19].

Ultra Wide Band (UWB) radar offers unique capabilities among the wide variety of remote sensing technologies. The ability to penetrate through non-metallic materials while retaining high resolution is of high interest in many application areas, including through-wall detection and identification of buried objects, and medical applications. There are many significant applications for UWB radar. The Ground Penetrating Radar (GPR) imaging is one of the most promising technologies for detection and identification of buried objects [16]. GPR is a specialized radar that can be used for producing images below the surface of the earth and makes use of optimized electromagnetic pulses that backscatter from objects below the ground that are being detected. Detection of buried objects is critical to safe operation when digging or operating vehicles around shale gas, oil, ground water and others. Due to many features of UWB radar such as penetration capability, high precision ranging, and low electromagnetic radiation, extensive research has been done for UWB medical applications in cardiology, obstetrics, breath cancer detection, breath pathways and arteries over the last decade [38]. Another important application is Through-the-wall radar (TWR) imaging. Through-the-wall radar imaging (TWRI) is emerging as a viable technology for providing high quality imagery of enclosed structures [33]. The technology highly available to detect and analyze through obstacles such as walls, doors, and other visually opaque materials for police, fire fighter, and rescuer. TWRI makes use of electromagnetic waves below the S-band to penetrate through building wall materials to not only determine if there are the targets inside a building structure but also to know where they are, with no direct vision of the inside. For instance, this technology is employed for surveillance and detection of humans and interior objects in urban environments (e.g. police or fire fighter rescuer teams obtain the information about human inside the building), and for search and rescue operations (e.g. when looking for people trapped inside buildings on fire or buried under rubble). In most applications of through-the-wall radar imaging, researchers are interested in human detection and analysis. Many sources have looked at using standard Doppler radar [35] or using through wall UWB radar [27] to study human beings periodic motions.

In scientific computation, numerical methods, such as Finite Difference method, Finite Element method, Finite Volume method, and Galerkin method, contribute great effort in solving Maxwell's equations [42]. Among various numerical approaches, finite difference method is often adopted in solving Maxwell's equations with different boundary conditions or initial conditions. In this dissertation, we exclusively investigate finite difference method.

The finite-difference time-domain (FDTD) method is a widely used numerical technique for solving the time domain Maxwell's equations of electrodynamics. The FDTD method is staggered in both space and time on rectangular grids. Each field component is sampled and evaluated at a particular space position and the magnetic and the electric fields are obtained at different instants of time delayed by half the sampling time step [51, 41]. The time-dependent Maxwell's equations (in differential form) are discretized using centered difference approximations. As an explicit numerical method, the FDTD method is subject to the Courant-Friedrichs-Lewy (CFL) stability condition [48, 40].

In [27], FDTD simulation and through wall radar experiment with UWB radar have been carried out for human being's periodic motion detection. In addition, advanced signal processing methods are presented to classify and to extract the human's periodic motion characteristic information, such as Micro-Doppler shift and motion frequency, from arm movement (isolated from torso movement) [30] to the small bodily fluctuations associated with breathing and heart beats [7]. Charnley et al. [11] used FDTD method to analyze objects inside a room, with no direct vision of the inside. In this dissertation, we apply the proposed temporal subcycling FDTD algorithm to simulate the TWR and employ a radar imaging method to reconstruct the object. In our case, we have tried one-transmitter multiple-receivers set-up and multiple-transmitters multiple-receivers set-up.

The accuracy and efficiency of the FDTD method can be significantly improved through the use of subgrids [1, 34, 37, 49, 52, 55], to selectively refine the grid in certain regions of the computation domain. In the last few decades there have been numerous investigations of subgridding and adaptive mesh refinement (AMR) algorithm strategies [24, 29, 43, 32, 12, 13, 54, 3, 28]. The main advantages of such methods are the reduced computational resource requirements and the increased computational efficiency over methods using uniform mesh when the region of interest occupies a small portion of the domain. The Huygens subgridding (HSG) technique [3] can achieve arbitrarily large of the ratio of the spatial steps, as illustrated in [3] with ratios as large as 99. However, these subgridding algorithms suffer from the late-time instablity problem. Numerical studies of this issue performed in the past such as [14, 24, 32, 36, 3] indicated that the stability of the subgridding algorithm is sensitive to the interpolation method and the choice of the interpolated fields. In [50], spatial and temporal mesh interfaces are separated in order to obtain better stability. In [28], a novel stable local spatial mesh refinement algorithm was developed based on the use invariant coordinate transformation of the Maxwell equations under logically rectangular grid and fully anisotropic FDTD method.

In this dissertation, we first investigate the stability of the subgridding FDTD methods and then propose a stable iteration based temporal subcycling FDTD algorithm. The subgridding FDTD method we focus on applies separated spatial and temporal mesh interfaces (as shown in Figure 1.1) so that the stability of spatial subgridding and temporal subcycling can be investigated independently. We study stability using update matrix eigenvalue analysis. We compute the largest eigenvalue of the update equations and perform long time simulation for millions of steps to verify the amplification of the solution. Our study shows that the spatial-only subgridding FDTD is stable while the temporal-only subcycling FDTD is late-time unstable as the amplification factor is slightly larger than 1. The Yee FDTD algorithm by itself is second order accurate and stable. However, due to the staggering grids in space and time, for the subgridding FDTD, the symmetry and positiveness of the update equations can be easily broken by the space-time interpolations required to produce the boundary conditions for the refined patches, i.e., the interpolation on the coarse/fine mesh interface. In order to overcome the late-time instability problem due to the temporal subcycling, we propose an iteration based temporal subcycling (ITS) FDTD algorithm. In general, as shown in Figure 1.1, we use refinement ratio 2:1 when designing and testing our subcycling algorithm. Our numerical results show that the iteration based temporal interpolation algorithm preserves the second-order accuracy of the original Yee scheme and is stable for long time simulation.

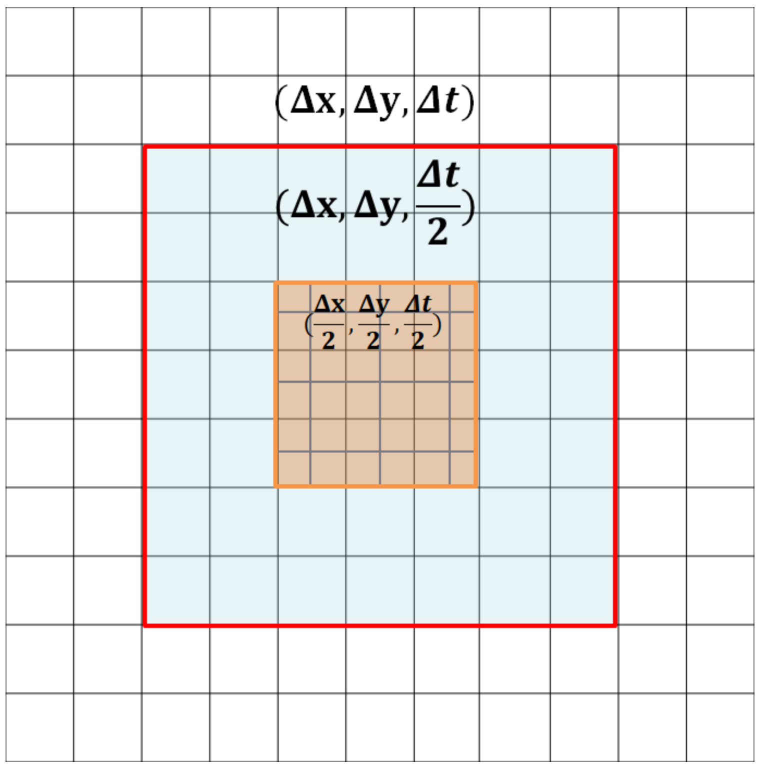

Figure 1.1: A two-dimensional subgridding mesh with separated spatial and temporal coarse/fine mesh interfaces.

The dissertation is organized as follows. Chapter 1 is the introduction. In Chapter 2, we review the FDTD method for solving Maxwell's equations and the spatial subgridding and temporal subcycling techniques. In Chapter 3, we present the proposed iteration based temporal subcycling algorithm. The through-the-wall radar imaging detection analysis in presented in Chapter 4. Chapter 5 shows numerical examples of different subgridding/subcycling methods and application to the through-the-wall radar simulations. Conclusion and future work are summarized in Chapter 6.

Chapter 2
THE FINITE-DIFFERENCE TIME-DOMAIN METHOD AND SUBGRIDDING TECHNIQUES

2.1 Finite-Difference Time-Domain Method

The Maxwell's equations of electrodynamics consist of Faraday's Law of induction, Ampère's Law, Gauss's Law for electric fields, and Gauss's Law for magnetic fields. These four laws can be written in differential form as a set of partial differential equations:

$$\begin{aligned} \nabla \times E &= -\frac{\partial B}{\partial t}, \\ \nabla \times H &= \frac{\partial D}{\partial t} + J, \\ \nabla \cdot D &= \rho, \\ \nabla \cdot B &= 0, \end{aligned} \tag{2.1}$$

where E and H represent the electric and magnetic fields, respectively; D and B represent the electric and magnetic flux densities, respectively; J and ρ terms are the current density and charge density. The constitutive relations between electric and magnetic fields and fluxes are

$$\begin{aligned} D &= \epsilon E, \\ B &= \mu H, \end{aligned} \tag{2.2}$$

where ϵ is the electric permittivity and μ is the magnetic permeability. The permittivity and permeability in free space are $\epsilon_0 = 8.854 \times 10^{-12}\ F/m$ and $\mu_0 = 4\pi \times 10^{-7}\ H/m$.

To illustrate the FDTD method, we consider the two dimensional Maxwell's equations in isotropic, homogeneous nondispersive media in transverse magnetic (TE_z) mode (ignorable z-coordinate)

$$\begin{aligned} \epsilon_0 \frac{\partial E_x}{\partial t} &= \frac{\partial H_z}{\partial y}, \\ \epsilon_0 \frac{\partial E_y}{\partial t} &= -\frac{\partial H_z}{\partial x}, \\ \mu_0 \frac{\partial H_z}{\partial t} &= \frac{\partial E_x}{\partial y} - \frac{\partial E_y}{\partial x}. \end{aligned} \tag{2.3}$$

The discretized update equations using Yee FDTD method is given by

$$E^{n+1}_{x\,i+\frac{1}{2},j} = E^{n}_{x\,i+\frac{1}{2},j} + (\frac{\Delta t}{\epsilon_0 \Delta y})(H^{n+\frac{1}{2}}_{z\,i+\frac{1}{2},j+\frac{1}{2}} - H^{n+\frac{1}{2}}_{z\,i+\frac{1}{2},j-\frac{1}{2}}), \tag{2.4}$$

$$E^{n+1}_{y\,i,j+\frac{1}{2}} = E^{n}_{y\,i,j+\frac{1}{2}} - (\frac{\Delta t}{\epsilon_0 \Delta x})(H^{n+\frac{1}{2}}_{z\,i+\frac{1}{2},j+\frac{1}{2}} - H^{n+\frac{1}{2}}_{z\,i-\frac{1}{2},j+\frac{1}{2}}), \tag{2.5}$$

$$\begin{aligned} H^{n+\frac{1}{2}}_{z\,i+\frac{1}{2},j+\frac{1}{2}} = H^{n-\frac{1}{2}}_{z\,i+\frac{1}{2},j+\frac{1}{2}} &+ (\frac{\Delta t}{\mu_0 \Delta y})(E^{n}_{x\,i+\frac{1}{2},j+1} - E^{n}_{x\,i+\frac{1}{2},j}) \\ &- (\frac{\Delta t}{\mu_0 \Delta x})(E^{n}_{y\,i+1,j+\frac{1}{2}} - E^{n}_{y\,i,j+\frac{1}{2}}), \end{aligned} \tag{2.6}$$

where Δt and Δx and Δy are the grid size in time and x and y spatial directions, respectively.

2.2 Perfectly Matched Layer Boundary Condition

It is necessary to apply a special boundary condition in order to absorb the outgoing waves. The perfectly matched layer (PML) is a very efficient absorbing boundary condition [2]. The PML technique allows the electromagnetic waves to be absorbed with a controllable reflection.

In this dissertation, we demonstrate and test our algorithms using the FDTD method in two-dimension with PML boundary condition in the TE_z case. The electromagnetic field involves four components, E_x, E_y, H_{zx}, H_{zy}, and the Maxwell's equations in two dimensions can be written as

$$\epsilon_0 \frac{\partial E_x}{\partial t} + \sigma_y E_x = \frac{\partial (H_{zx} + H_{zy})}{\partial y}, \tag{2.7}$$

$$\epsilon_0 \frac{\partial E_y}{\partial t} + \sigma_x E_y = -\frac{\partial (H_{zx} + H_{zy})}{\partial x}, \tag{2.8}$$

$$\mu_0 \frac{\partial H_{zx}}{\partial t} + \sigma^*_x H_{zx} = -\frac{\partial E_y}{\partial x}, \tag{2.9}$$

$$\mu_0 \frac{\partial H_{zy}}{\partial t} + \sigma^*_y H_{zy} = \frac{\partial E_x}{\partial y}. \tag{2.10}$$

where the parameters σ_x and σ_y are electric conductivities; σ^*_x and σ^*_y are magnetic conductivities. If $\sigma_x^* = \sigma_y^*$, then equation (2.7) to equation (2.10) can reduces to a set of three equations involving three components E_x, E_y, and $H_z = H_{zx} + H_{zy}$.

2.3 Spatial Subgridding

First, we introduce the spatial subgridding FDTD method, where the computational domain contains a coarse grid and a fine grid, as shown in Figure 2.1. The FDTD method is applied to solve the Maxwell's equations on the coarse and fine meshes, and interpolation is required on the calculation of the fields near the bounday of the fine grid (the interface between coarse and fine meshes). Here, we set the ratio of the coarse and fine region grid sizes to be 2:1, so the solution on the fine mesh needs to be updated twice when the solutions on the coarse region advances for one time step. For simplicity, we assume that the mesh is uniform along each co-ordinate direction, but the scheme can be straightforwardly extended to non-uniform meshes [43]. In the following discussion we show two interpolation algorithms for 2D TE_z mode.

For example, if we want to calculate the magnetic fields on fine region boundary, we need to interpolate the missing values using the coarse region magnetic fields due to boundary truncation. The missing values are the ghost values on fine mesh boundary. It similar interpolation can be applied to the electric field. The interpolation methods are presented in the following subsections. The ratio of the mesh cell size of the main grid and subgrid is 1:2, meaning that the mesh cell size in the main grid is Δx and Δy and in the subgrid is $\Delta x/2$ and $\Delta y/2$. Same Δt is used when updating coarse and fine meshes.

In the following discussions, we show two ways of interpolating H ghost values. These two interpolations are the spatial subgridding algorithm with Ghost H field on Coarse mesh (GHC) method and the spatial subgridding algorithm with Ghost H field on Fine mesh (GHF) method.

2.3.1 The spatial subgridding algorithm with GHC

In the first case, we consider the case where the ghost boundary values is in the coarse region as shown in Figure 2.2. We assume the magnetic field is in the center of the grid cell and the electric

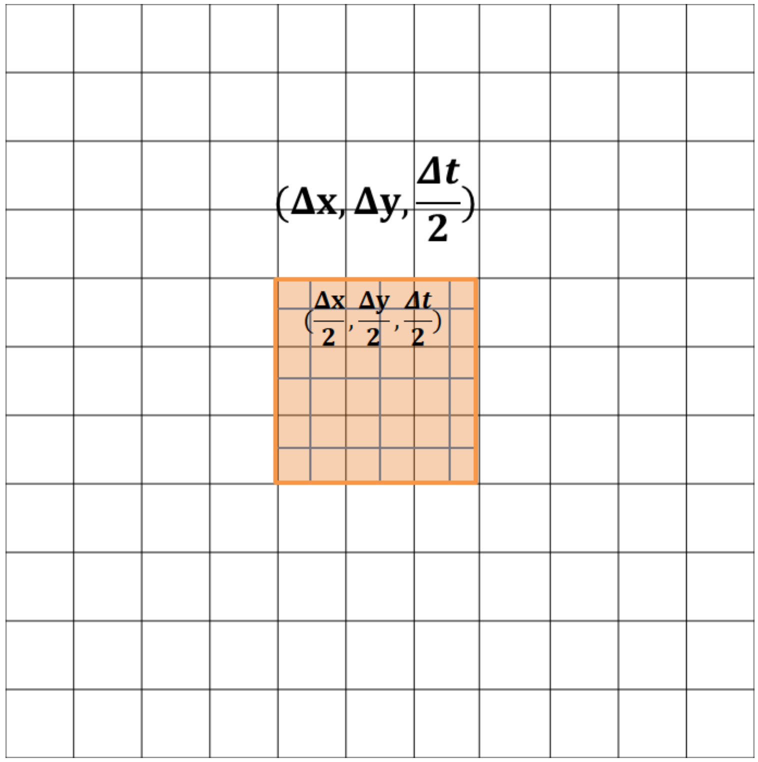

Figure 2.1: A two-dimensional spatial subgridding mesh with spatial coarse/fine mesh ratio 2:1.

field is along the grid cell boundaries. In the coarse region, the magnetic field value is denoted by H_{zc} and the electric field values are denoted by E_{xc} and E_{yc}. In the fine region, the magnetic field value is denoted by H_{fz} and the electric field values are denoted by E_{fx} and E_{fy}, and the ghost boundary value is denoted by $\hat{H}_{fz}$.

Referring to the Fig. 2.2 which depict a regular coarse-fine region boundary and defining update as application of the Yee scheme equations (2.4)-(2.6), the algorithm can be summarized by the following steps:

1. Update H_{zc} on the coarse mesh, from time step $n - \frac{1}{2}$ to $n + \frac{1}{2}$.

$$H^{n+\frac{1}{2}}_{zc\,i+\frac{1}{2},j+\frac{1}{2}} \leftarrow H^{n-\frac{1}{2}}_{zc\,i+\frac{1}{2},j+\frac{1}{2}},\ by\ using\ E^{n}_{xc\,i+\frac{1}{2},j+1}, E^{n}_{xc\,i+\frac{1}{2},j}, E^{n}_{yc\,i+1,j+\frac{1}{2}}, E^{n}_{yc\,i,j+\frac{1}{2}}$$

2. Update E_{xc} and E_{yc} on the coarse mesh, from n to $n+1$.

$$E^{n+1}_{xc\ i+\frac{1}{2},j} \leftarrow E^{n}_{xc\ i+\frac{1}{2},j},\ by\ using\ H^{n+\frac{1}{2}}_{zc\ i+\frac{1}{2},j+\frac{1}{2}}, H^{n+\frac{1}{2}}_{zc\ i+\frac{1}{2},j-\frac{1}{2}}$$
$$E^{n+1}_{yc\ i,j+\frac{1}{2}} \leftarrow E^{n}_{yc\ i,j+\frac{1}{2}},\ by\ using\ H^{n+\frac{1}{2}}_{zc\ i+\frac{1}{2},j+\frac{1}{2}}, H^{n+\frac{1}{2}}_{zc\ i-\frac{1}{2},j+\frac{1}{2}}$$

3. Interpolate magnetic field ghost values $\hat{H}_{fz\ i-\frac{1}{4},j-\frac{1}{4}}$, $\hat{H}_{fz\ i+\frac{1}{4},j-\frac{1}{4}}$ and $\hat{H}_{fz\ i-\frac{1}{4},j+\frac{1}{4}}$ using coarse mesh $H_{zc\ i-\frac{1}{2},j-\frac{1}{2}}$, $H_{zc\ i+\frac{1}{2},j-\frac{1}{2}}$, $H_{zc\ i-\frac{1}{2},j+\frac{1}{2}}$ and $H_{zc\ i+\frac{1}{2},j+\frac{1}{2}}$ at time $n+\frac{1}{2}$.

4. Update H_{fz} on the fine mesh, from $n-\frac{1}{2}$ to $n+\frac{1}{2}$.

$$H^{n+\frac{1}{2}}_{fz\ i+\frac{1}{4},j+\frac{1}{4}} \leftarrow H^{n-\frac{1}{2}}_{fz\ i+\frac{1}{4},j+\frac{1}{4}},\ by\ using\ E^{n}_{fx\ i+\frac{1}{4},j+\frac{1}{2}}, E^{n}_{fx\ i+\frac{1}{4},j}, E^{n}_{fy\ i+\frac{1}{2},j+\frac{1}{4}}, E^{n}_{fy\ i,j+\frac{1}{4}}$$

5. Update E_{fx} and E_{fy} on the fine mesh, from n to $n+1$.

$$E^{n+1}_{fx\ i+\frac{1}{4},j} \leftarrow E^{n}_{fx\ i+\frac{1}{4},j},\ by\ using\ H^{n+\frac{1}{2}}_{fz\ i+\frac{1}{4},j+\frac{1}{4}}, H^{n+\frac{1}{2}}_{fz\ i+\frac{1}{4},j-\frac{1}{4}}$$
$$E^{n+1}_{fy\ i,j+\frac{1}{4}} \leftarrow E^{n}_{fy\ i,j+\frac{1}{4}},\ by\ using\ H^{n+\frac{1}{2}}_{fz\ i+\frac{1}{4},j+\frac{1}{4}}, H^{n+\frac{1}{2}}_{fz\ i-\frac{1}{4},j+\frac{1}{4}}$$

6. Replace H_{zc} magnetic field by H_{fz} in the region where fine grid overlaps coarse grid:

$$H^{n+\frac{1}{2}}_{zc\ i+\frac{1}{2},j+\frac{1}{2}} = \frac{1}{4}(H^{n+\frac{1}{2}}_{fz\ i+\frac{1}{4},j+\frac{1}{4}} + H^{n+\frac{1}{2}}_{fz\ i+\frac{3}{4},j+\frac{1}{4}} + H^{n+\frac{1}{2}}_{fz\ i+\frac{1}{4},j+\frac{3}{4}} + H^{n+\frac{1}{2}}_{fz\ i+\frac{3}{4},j+\frac{3}{4}}).$$

7. Update E_{xc} and E_{yc} on the coarse mesh as in step 2.

These steps are applied recursively at each refinement level. In our formulation the magnetic field is interpolated to obtain the ghost cell values. Therefore, electric field values at the interface can be computed using the same Yee algorithm as in the interior. $E_{xc\ i+\frac{1}{2},j+1}$, $E_{xc\ i+\frac{1}{2},j}$, $E_{yc\ i+1,j+\frac{1}{2}}$ and $E_{yc\ i,j+\frac{1}{2}}$ in the unit cell of coarse region are updated from time step n to $n+1$, while $H_{zc\ i+\frac{1}{2},j+\frac{1}{2}}$ is updated from time step $n-1/2$ to $n+1/2$. Each unit cell in the fine region is divided into four equal small cells as shown in Figure 2.2. E_{fx}, E_{fy} and H_{fz} in each unit cell of fine region is updated

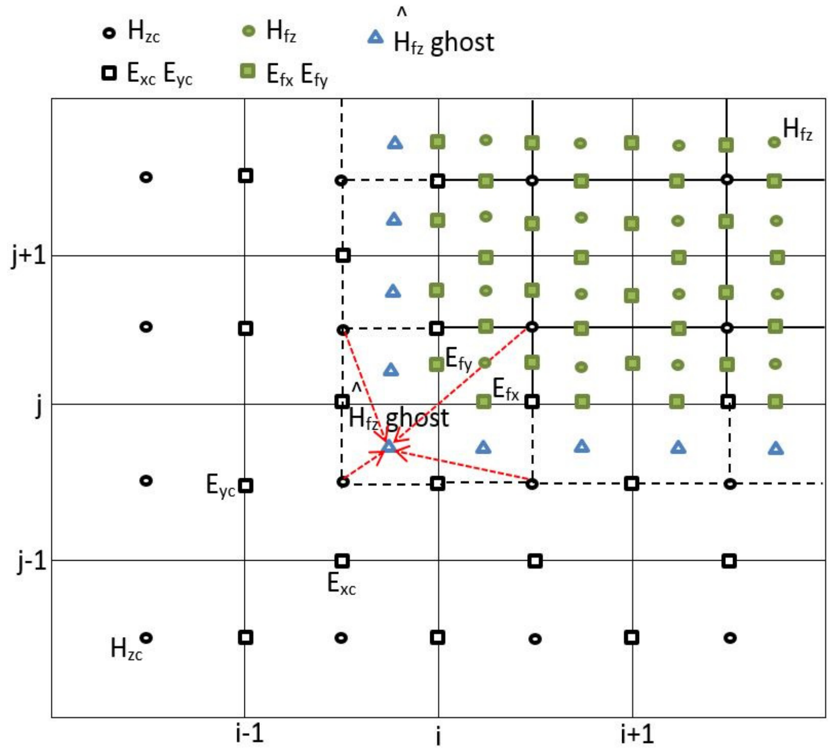

Figure 2.2: The spatial subgridding with GHC for TE_z mode. Blue triangles denote boundary values of the magnetic ghost values.

using the same FDTD algorithm. After updating H_{fz} filed, we use the space averaged H_{fz} fileds to replace H_{zc} field in each unit cell of the coarse region where it overlaps with the fine region [5] in step 6. The final step is to re-update the electric field by using the new magnetic field values from the previous step on the coarse grid. In order to calculate the fine region boundary electric field, we need to use the coarse magnetic field to interpolate the missing fine region magnetic field values.

In step 3, the magnetic field ghost value is interpolated from coarse mesh as follows,

$$\hat{H}^{n+\frac{1}{2}}_{fz\,i+\frac{1}{4},j-\frac{1}{4}} = \frac{5}{8}H^{n+\frac{1}{2}}_{zc\,i+\frac{1}{2},j-\frac{1}{2}} + \frac{1}{8}H^{n+\frac{1}{2}}_{zc\,i+\frac{1}{2},j+\frac{1}{2}} + \frac{1}{8}H^{n+\frac{1}{2}}_{zc\,i-\frac{1}{2},j+\frac{1}{2}} + \frac{1}{8}H^{n+\frac{1}{2}}_{zc\,i-\frac{1}{2},j-\frac{1}{2}}, \tag{2.11}$$

$$\hat{H}^{n+\frac{1}{2}}_{fz\,i-\frac{1}{4},j+\frac{1}{4}} = \frac{5}{8}H^{n+\frac{1}{2}}_{zc\,i-\frac{1}{2},j+\frac{1}{2}} + \frac{1}{8}H^{n+\frac{1}{2}}_{zc\,i+\frac{1}{2},j+\frac{1}{2}} + \frac{1}{8}H^{n+\frac{1}{2}}_{zc\,i+\frac{1}{2},j-\frac{1}{2}} + \frac{1}{8}H^{n+\frac{1}{2}}_{zc\,i-\frac{1}{2},j-\frac{1}{2}}, \tag{2.12}$$

$$\hat{H}^{n+\frac{1}{2}}_{fz\,i-\frac{1}{4},j-\frac{1}{4}} = \frac{5}{8}H^{n+\frac{1}{2}}_{zc\,i-\frac{1}{2},j-\frac{1}{2}} + \frac{1}{8}H^{n+\frac{1}{2}}_{zc\,i+\frac{1}{2},j+\frac{1}{2}} + \frac{1}{8}H^{n+\frac{1}{2}}_{zc\,i+\frac{1}{2},j-\frac{1}{2}} + \frac{1}{8}H^{n+\frac{1}{2}}_{zc\,i-\frac{1}{2},j+\frac{1}{2}}. \tag{2.13}$$

Interpolation in space is done using linear interpolation, as in equations (2.11)-(2.13). This linear interpolation is used to calculate each ghost boundary value inside a dual cell with H_{zc} as four corners. There is different way of the interpolation with different coefficients of neighboring H_{zc}, e.g.:

$$\hat{H}^{n+\frac{1}{2}}_{fz\,i+\frac{1}{4},j-\frac{1}{4}} = \frac{9}{16}H^{n+\frac{1}{2}}_{zc\,i+\frac{1}{2},j-\frac{1}{2}} + \frac{3}{16}H^{n+\frac{1}{2}}_{zc\,i+\frac{1}{2},j+\frac{1}{2}} + \frac{3}{16}H^{n+\frac{1}{2}}_{zc\,i-\frac{1}{2},j-\frac{1}{2}} + \frac{1}{16}H^{n+\frac{1}{2}}_{zc\,i-\frac{1}{2},j+\frac{1}{2}}. \tag{2.14}$$

Although the algorithm is given for a grid refinement ratio 1:2, it can be extended to higher ratios.

2.3.2 The spatial subgridding algorithm with GHF

In the second case, we consider that the ghost boundary values is in the fine region as shown in Figure 2.3. Similar to the previous case, the magnetic field is in the center of the grid cell and the electric field is along the grid cell boundaries. In the coarse region, the magnetic field value and the electric field values are denoted by H_{zc}, E_{xc} and E_{yc}. The magnetic field value and the electric field values are denoted by H_{fz}, E_{fx} and E_{fy} in the fine region, and the ghost boundary value is denoted by $\hat{H}_{fz}$.

Referring to the Fig. 2.3, the algorithm can be summarized by the following steps:

1. Update H_{zc} on the coarse mesh, form $n-\frac{1}{2}$ to $n+\frac{1}{2}$.

$$H^{n+\frac{1}{2}}_{zc\,i+\frac{1}{2},j+\frac{1}{2}} \leftarrow H^{n-\frac{1}{2}}_{zc\,i+\frac{1}{2},j+\frac{1}{2}},\ by\ using\ E^{n}_{xc\,i+\frac{1}{2},j+1}, E^{n}_{xc\,i+\frac{1}{2},j}, E^{n}_{yc\,i+1,j+\frac{1}{2}}, E^{n}_{yc\,i,j+\frac{1}{2}}$$

2. Update E_{xc} and E_{yc} on the coarse mesh, from n to $n+1$.

$$E^{n+1}_{xc\,i+\frac{1}{2},j} \leftarrow E^{n}_{xc\,i+\frac{1}{2},j},\ by\ using\ H^{n+\frac{1}{2}}_{zc\,i+\frac{1}{2},j+\frac{1}{2}}, H^{n+\frac{1}{2}}_{zc\,i+\frac{1}{2},j-\frac{1}{2}}$$
$$E^{n+1}_{yc\,i,j+\frac{1}{2}} \leftarrow E^{n}_{yc\,i,j+\frac{1}{2}},\ by\ using\ H^{n+\frac{1}{2}}_{zc\,i+\frac{1}{2},j+\frac{1}{2}}, H^{n+\frac{1}{2}}_{zc\,i-\frac{1}{2},j+\frac{1}{2}}$$

3. Interpolate magnetic field ghost values $\hat{H}_{fz\,i+\frac{1}{4},j+\frac{1}{4}}$, $\hat{H}_{fz\,i+\frac{3}{4},j+\frac{1}{4}}$ and $\hat{H}_{fz\,i+\frac{1}{4},j+\frac{3}{4}}$ using coarse mesh $H_{zc\,i-\frac{1}{2},j-\frac{1}{2}}$, $H_{zc\,i+\frac{1}{2},j-\frac{1}{2}}$, $H_{zc\,i-\frac{1}{2},j+\frac{1}{2}}$, $H_{zc\,i+\frac{1}{2},j+\frac{1}{2}}$, $H_{zc\,i+\frac{3}{2},j-\frac{1}{2}}$, $H_{zc\,i+\frac{3}{2},j+\frac{1}{2}}$, $H_{zc\,i-\frac{1}{2},j+\frac{3}{2}}$ and $H_{zc\,i+\frac{1}{2},j+\frac{3}{2}}$ at time $n+\frac{1}{2}$.

4. Update H_{fz} on the fine mesh, from $n-\frac{1}{2}$ to $n+\frac{1}{2}$.

$$H^{n+\frac{1}{2}}_{fz\,i+\frac{3}{4},j+\frac{3}{4}} \leftarrow H^{n-\frac{1}{2}}_{fz\,i+\frac{3}{4},j+\frac{3}{4}},\ \textit{by using}\ E^{n}_{fx\,i+\frac{3}{4},j+\frac{1}{2}}, E^{n}_{fx\,i+\frac{3}{4},j+1}, E^{n}_{fy\,i+\frac{1}{2},j+\frac{3}{4}}, E^{n}_{fy\,i+1,j+\frac{3}{4}}$$

5. Update E_{fx} and E_{fy} on the fine mesh, from n to $n+1$.

$$E^{n+1}_{fx\,i+\frac{3}{4},j+\frac{1}{2}} \leftarrow E^{n}_{fx\,i+\frac{3}{4},j+\frac{1}{2}},\ \textit{by using}\ H^{n+\frac{1}{2}}_{fz\,i+\frac{3}{4},j+\frac{3}{4}}, H^{n+\frac{1}{2}}_{fz\,i+\frac{3}{4},j+\frac{1}{4}}$$
$$E^{n+1}_{fy\,i+\frac{1}{2},j+\frac{3}{4}} \leftarrow E^{n}_{fy\,i+\frac{1}{2},j+\frac{3}{4}},\ \textit{by using}\ H^{n+\frac{1}{2}}_{fz\,i+\frac{3}{4},j+\frac{3}{4}}, H^{n+\frac{1}{2}}_{fz\,i+\frac{1}{4},j+\frac{3}{4}}$$

6. Replace H_{zc} magnetic field by H_{fz} in the region where fine grid overlaps coarse grid:

$$H^{n+\frac{1}{2}}_{zc\,i+\frac{1}{2},j+\frac{1}{2}} = \frac{1}{4}(H^{n+\frac{1}{2}}_{fz\,i+\frac{1}{4},j+\frac{1}{4}} + H^{n+\frac{1}{2}}_{fz\,i+\frac{3}{4},j+\frac{1}{4}} + H^{n+\frac{1}{2}}_{fz\,i+\frac{1}{4},j+\frac{3}{4}} + H^{n+\frac{1}{2}}_{fz\,i+\frac{3}{4},j+\frac{3}{4}}).$$

7. Update E_{xc} and E_{yc} on the coarse mesh as in step 2.

Similar to the first case, $E_{xc\,i+\frac{1}{2},j+1}$, $E_{xc\,i+\frac{1}{2},j}$, $E_{yc\,i+1,j+\frac{1}{2}}$ and $E_{yc\,i,j+\frac{1}{2}}$ in the unit cell of coarse region are updated from time n to $n+1$, while $H_{zc\,i+\frac{1}{2},j+\frac{1}{2}}$ is updated from time step $n-1/2$ to $n+1/2$. The original unit cell in the fine region is divided into four equal small cells as shown in Figure 2.3. However, the location of the ghost boundary values differ from the previous case. The final step is to recalculate the electric field by using the modified magnetic field values from the previous step on the coarse grid. In order to calculate the fine region boundary electric field, we need to use the coarse magnetic field to interpolate the missing fine region magnetic field values.

In step 3, the magnetic field ghost value is interpolated from coarse mesh:

$$\hat{H}^{n+\frac{1}{2}}_{fz\,i+\frac{1}{4},j+\frac{1}{4}} = \frac{5}{8}H^{n+\frac{1}{2}}_{zc\,i+\frac{1}{2},j+\frac{1}{2}} + \frac{1}{8}H^{n+\frac{1}{2}}_{zc\,i+\frac{1}{2},j-\frac{1}{2}} + \frac{1}{8}H^{n+\frac{1}{2}}_{zc\,i-\frac{1}{2},j+\frac{1}{2}} + \frac{1}{8}H^{n+\frac{1}{2}}_{zc\,i-\frac{1}{2},j-\frac{1}{2}}, \tag{2.15}$$

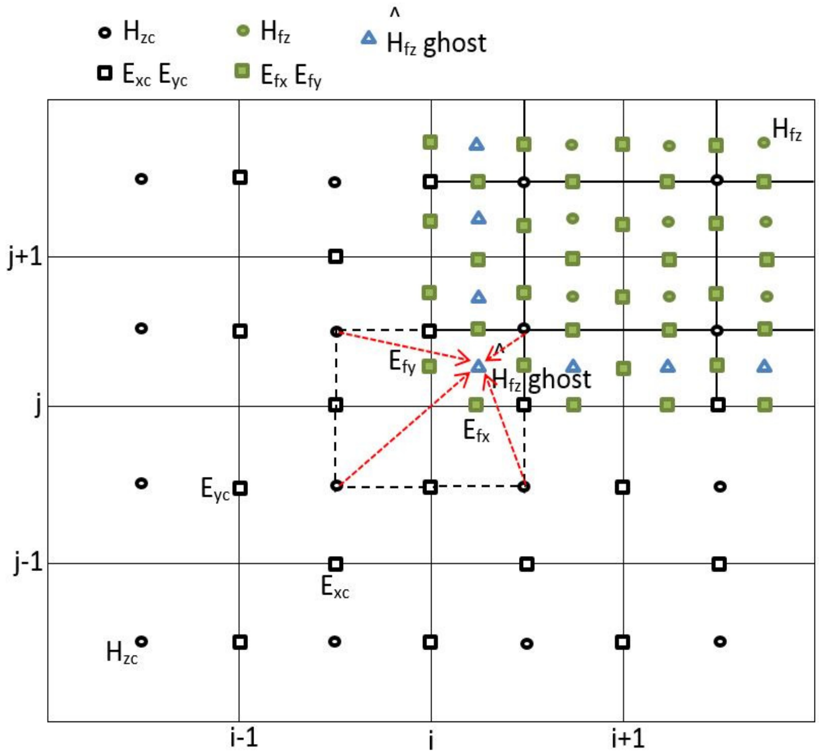

Figure 2.3: The spatial subgridding with GHF for TE_z mode. Blue triangles denote boundary values of the magnetic ghost values.

$$\hat{H}^{n+\frac{1}{2}}_{fz\,i+\frac{3}{4},j+\frac{1}{4}} = \frac{5}{8}H^{n+\frac{1}{2}}_{zc\,i+\frac{1}{2},j+\frac{1}{2}} + \frac{1}{8}H^{n+\frac{1}{2}}_{zc\,i+\frac{1}{2},j-\frac{1}{2}} + \frac{1}{8}H^{n+\frac{1}{2}}_{zc\,i+\frac{3}{2},j+\frac{1}{2}} + \frac{1}{8}H^{n+\frac{1}{2}}_{zc\,i+\frac{3}{2},j-\frac{1}{2}}, \tag{2.16}$$

$$\hat{H}^{n+\frac{1}{2}}_{fz\,i+\frac{1}{4},j+\frac{3}{4}} = \frac{5}{8}H^{n+\frac{1}{2}}_{zc\,i+\frac{1}{2},j+\frac{1}{2}} + \frac{1}{8}H^{n+\frac{1}{2}}_{zc\,i-\frac{1}{2},j+\frac{1}{2}} + \frac{1}{8}H^{n+\frac{1}{2}}_{zc\,i+\frac{1}{2},j+\frac{3}{2}} + \frac{1}{8}H^{n+\frac{1}{2}}_{zc\,i-\frac{1}{2},j+\frac{3}{2}}. \tag{2.17}$$

Interpolation in space is done using linear interpolation, as in equations (2.15)-(2.17). The linear interpolation is used to calculate each ghost boundary value inside a dual cell with H_{zc} as four corners. There is different way of the interpolation with different coefficient of H_{zc}, e.g.:

$$\hat{H}^{n+\frac{1}{2}}_{fz\,i+\frac{1}{4},j+\frac{1}{4}} = \frac{9}{16}H^{n+\frac{1}{2}}_{zc\,i+\frac{1}{2},j+\frac{1}{2}} + \frac{3}{16}H^{n+\frac{1}{2}}_{zc\,i+\frac{1}{2},j-\frac{1}{2}} + \frac{3}{16}H^{n+\frac{1}{2}}_{zc\,i-\frac{1}{2},j+\frac{1}{2}} + \frac{1}{16}H^{n+\frac{1}{2}}_{zc\,i-\frac{1}{2},j-\frac{1}{2}}. \tag{2.18}$$

This algorithm also can be extended to higher ratios. The numerical examinations in Chapter 5 show that this GHF interpolation method has better stability than the previous spatial subgridding with GHC method. In the through-the-wall radar simulation, we will use this subgrid algorithm instead of the one presented in the previous section.

2.4 Temporal Subcycling

In this section, we consider a temporal subcycling technique for the FDTD method. Similar to the spatial subgridding method, the original Yee FDTD method is used to calculate the fields in the coarse grids and in the fine grids. With different time steps, the coarse region and fine region have different temporal steps. Each of them needs to run with a different time-step in order to satisfy their respective stability conditions. Hence, the challenging issue for the use of subcycling techniques in FDTD modeling is the handling of temporal interpolation of the boundaries between the main coarse grid and the fine subgrid as shown in Figure 2.4.

We use the standard FDTD update equations (2.4)-(2.6) in the coarse and fine regions. Due to the boundary truncation, we need to calculate the missing values at the interface between the coarse region and fine region. The missing values are the ghost boundary values on the fine mesh. The interpolation methods for ghost value calculation are presented in the following subsections. Due to the ratio of the time steps of the main grid and subgrid is 1:2, meaning that time step in the main grid is Δt and in the subgrid is $\Delta t/2$. In other words, two FDTD sub-iterations are performed during every main grid iteration. We denote n as the index on time in the main grid, so that $n \to n+1$ is an advance by Δt and $n \to n+1/2$ is an advance by $\Delta t/2$.

2.4.1 The temporal subcycling algorithm with GH

Referring to the Fig. 2.5, the temporal subcycling algorithm with ghost H_z fields (GH) in 2D TE_z mode can be summarized by the following steps:

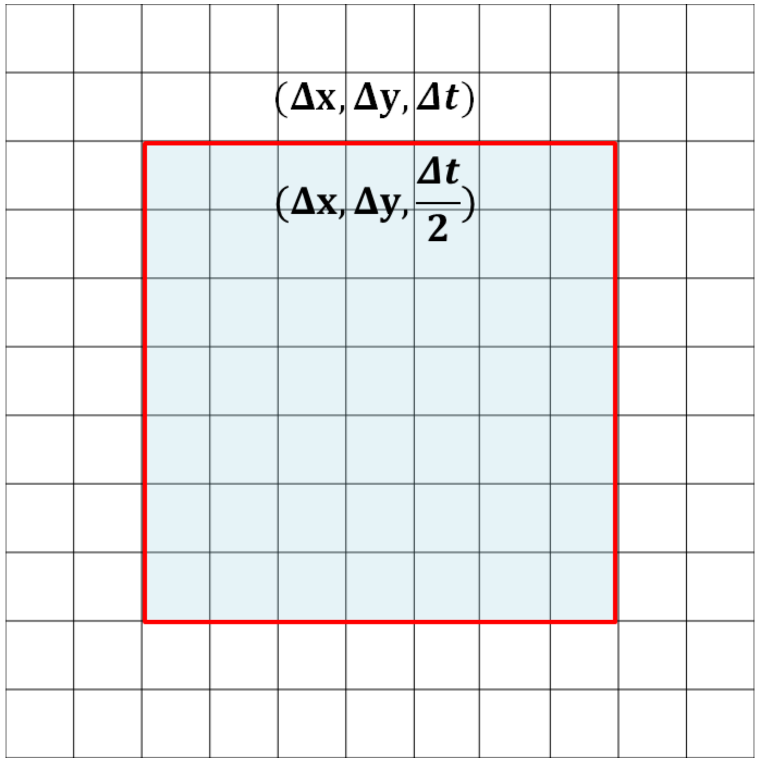

Figure 2.4: A two-dimensional temporal subcycling mesh with temporal coarse/fine mesh ratio 2:1.

1. Update H_{zc} on the coarse mesh, from $n - \frac{1}{2}$ to $n + \frac{1}{2}$.

$$H^{n+\frac{1}{2}}_{zc\, i+\frac{1}{2},j+\frac{1}{2}} \leftarrow H^{n-\frac{1}{2}}_{zc\, i+\frac{1}{2},j+\frac{1}{2}},\ by\ using\ E^{n}_{xc\, i+\frac{1}{2},j+1}, E^{n}_{xc\, i+\frac{1}{2},j}, E^{n}_{yc\, i+1,j+\frac{1}{2}}, E^{n}_{yc\, i,j+\frac{1}{2}}$$

2. Update E_{xc} and E_{yc} on the coarse mesh, from n to $n + 1$.

$$E^{n+1}_{xc\, i+\frac{1}{2},j} \leftarrow E^{n}_{xc\, i+\frac{1}{2},j},\ by\ using\ H^{n+\frac{1}{2}}_{zc\, i+\frac{1}{2},j+\frac{1}{2}}, H^{n+\frac{1}{2}}_{zc\, i+\frac{1}{2},j-\frac{1}{2}}$$
$$E^{n+1}_{yc\, i,j+\frac{1}{2}} \leftarrow E^{n}_{yc\, i,j+\frac{1}{2}},\ by\ using\ H^{n+\frac{1}{2}}_{zc\, i+\frac{1}{2},j+\frac{1}{2}}, H^{n+\frac{1}{2}}_{zc\, i-\frac{1}{2},j+\frac{1}{2}}$$

3. Interpolate magnetic field ghost value $\hat{H}^{n}_{zf}$ using coarse mesh $H^{n-\frac{1}{2}}_{zc}$ and $H^{n+\frac{1}{2}}_{zc}$.

4. Update H_{zf} on the fine mesh, from $n - \frac{1}{2}$ to n.

$$H^{n}_{zf\ i+\frac{1}{2},j+\frac{1}{2}} \leftarrow H^{n-\frac{1}{2}}_{zf\ i+\frac{1}{2},j+\frac{1}{2}},\ by\ using\ E^{n-\frac{1}{4}}_{xf\ i+\frac{1}{2},j+1}, E^{n-\frac{1}{4}}_{xf\ i+\frac{1}{2},j}, E^{n-\frac{1}{4}}_{yf\ i+1,j+\frac{1}{2}}, E^{n-\frac{1}{4}}_{yf\ i,j+\frac{1}{2}}$$

5. Update E_{xf} and E_{yf} on the fine mesh, $n - \frac{1}{4}$ to $n + \frac{1}{4}$.

$$E^{n+\frac{1}{4}}_{xf\ i+\frac{1}{2},j} \leftarrow E^{n-\frac{1}{4}}_{xf\ i+\frac{1}{2},j},\ by\ using\ H^{n}_{zf\ i+\frac{1}{2},j+\frac{1}{2}}, H^{n}_{zf\ i+\frac{1}{2},j-\frac{1}{2}}$$
$$E^{n+\frac{1}{4}}_{yf\ i,j+\frac{1}{2}} \leftarrow E^{n-\frac{1}{4}}_{yf\ i,j+\frac{1}{2}},\ by\ using\ H^{n}_{zf\ i+\frac{1}{2},j+\frac{1}{2}}, H^{n}_{zf\ i-\frac{1}{2},j+\frac{1}{2}}$$

6. Interpolate magnetic field ghost value $\hat{H}^{n+\frac{1}{2}}_{zf}$ using coarse mesh $H^{n+\frac{1}{2}}_{zc}$.

7. Update H_{zf} on the fine mesh, from n to $n + \frac{1}{2}$.

$$H^{n+\frac{1}{2}}_{zf\ i+\frac{1}{2},j+\frac{1}{2}} \leftarrow H^{n}_{zf\ i+\frac{1}{2},j+\frac{1}{2}},\ by\ using\ E^{n+\frac{1}{4}}_{xf\ i+\frac{1}{2},j+1}, E^{n+\frac{1}{4}}_{xf\ i+\frac{1}{2},j}, E^{n+\frac{1}{4}}_{yf\ i+1,j+\frac{1}{2}}, E^{n+\frac{1}{4}}_{yf\ i,j+\frac{1}{2}}$$

8. Update E_{xf} and E_{yf} on the fine mesh, from $n + \frac{1}{4}$ to $n + \frac{3}{4}$.

$$E^{n+\frac{3}{4}}_{xf\ i+\frac{1}{2},j} \leftarrow E^{n+\frac{1}{4}}_{xf\ i+\frac{1}{2},j},\ by\ using\ H^{n+\frac{1}{2}}_{zf\ i+\frac{1}{2},j+\frac{1}{2}}, H^{n+\frac{1}{2}}_{zf\ i+\frac{1}{2},j-\frac{1}{2}}$$
$$E^{n+\frac{3}{4}}_{yf\ i,j+\frac{1}{2}} \leftarrow E^{n+\frac{1}{4}}_{yf\ i,j+\frac{1}{2}},\ by\ using\ H^{n+\frac{1}{2}}_{zf\ i+\frac{1}{2},j+\frac{1}{2}}, H^{n+\frac{1}{2}}_{zf\ i-\frac{1}{2},j+\frac{1}{2}}$$

9. Replace H_{zc} magnetic field by H_{zf} in the region where fine grid overlaps coarse grid:

$$H^{n+\frac{1}{2}}_{zc\ i+\frac{1}{2},j+\frac{1}{2}} = H^{n+\frac{1}{2}}_{zf\ i+\frac{1}{2},j+\frac{1}{2}}.$$

10. Update E_{xc} and E_{yc} on the coarse mesh as in step 2.

The above steps are applied recursively at each refinement level. The ghost cell values of the magnetic field is obtained by interpolation using neighboring values. All electric field values in the fine mesh region are computed using the standard Yee algorithm. On the coarse grid, H_{zc} field is

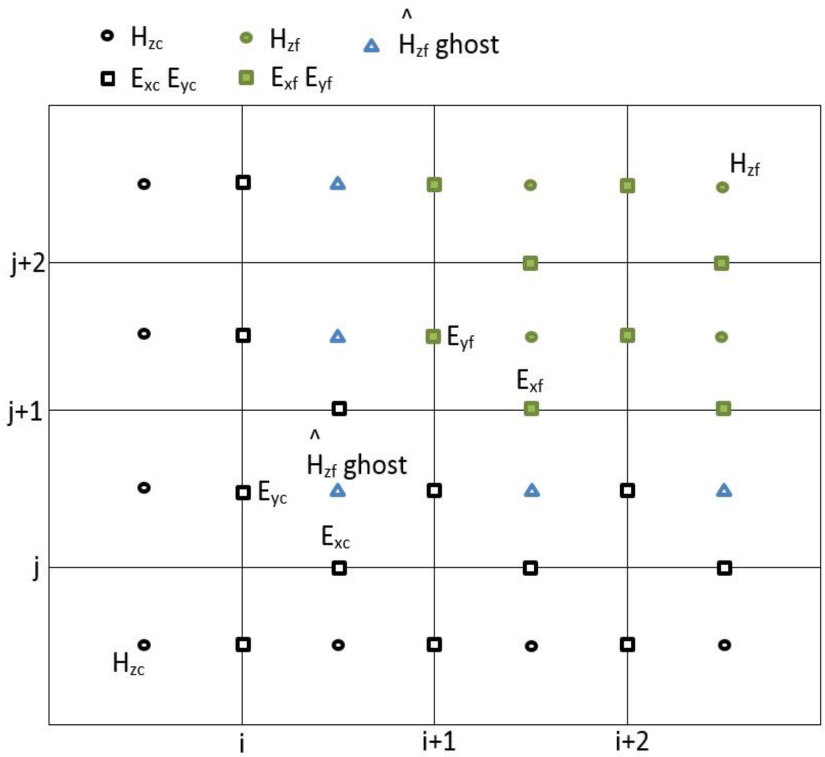

Figure 2.5: The temporal subcycling with GH for TE_z mode. Blue triangles denote the magnetic ghost values on the fine mesh boundary.

updated from time step $n-1/2$ to $n+1/2$, followed by E_{xc} and E_{yc} fields update from time step n to $n+1$. In the meanwhile, the fine mesh solutions are updated twice: first update of H_{zf} is from $n-1/2$ to n, followed by E_{xf} and E_{yf} update from $n-1/4$ to $n+1/4$; then the second update of H_{zf} from n to $n+1/2$, followed by the update of E_{xf} and E_{yf} from $n+1/4$ to $n+3/4$. The interpolation of the magnetic field on the coarse grid by the time averaged magnetic fields on the fine grid at the interface is done in step 9. The step 10 is to recalculate the electric filed by using the new magnetic filed values obtained from step 9 in the coarse region.

In step 3, the magnetic field ghost values are interpolated from coarse mesh:

$$\hat{H}^{n}_{zf\ i+\frac{1}{2},j+\frac{1}{2}} = \frac{1}{2}(H^{n-\frac{1}{2}}_{zc\ i+\frac{1}{2},j+\frac{1}{2}} + H^{n+\frac{1}{2}}_{zc\ i+\frac{1}{2},j+\frac{1}{2}}). \tag{2.19}$$

Similarly, in step 6, the magnetic field ghost values are interpolated from coarse mesh:

$$\hat{H}^{n+\frac{1}{2}}_{zf\ i+\frac{1}{2},j+\frac{1}{2}} = H^{n+\frac{1}{2}}_{zc\ i+\frac{1}{2},j+\frac{1}{2}}. \tag{2.20}$$

Although the algorithm is given for a grid refinement ratio 1:2, it can be extended to higher ratios.

2.4.2 The temporal subcycling algorithm with GE

The electric field ghost value interpolation is slightly more complicated than the magnetic field interpolation shown in the previous section, since there are two electric field components $\hat{E}_{xf}$ and $\hat{E}_{yf}$ for TE_z mode. Referring to the Fig. 2.6 and using Yee update equations (2.4)-(2.6), the algorithm can be summarized by the following steps:

1. Update E_{xc} and E_{yc} on the coarse mesh, from $n-\frac{1}{2}$ to $n+\frac{1}{2}$.

$$\begin{aligned} E^{n+\frac{1}{2}}_{xc\ i+\frac{1}{2},j} &\leftarrow E^{n-\frac{1}{2}}_{xc\ i+\frac{1}{2},j},\ \textit{by using } H^{n}_{zc\ i+\frac{1}{2},j+\frac{1}{2}}, H^{n}_{zc\ i+\frac{1}{2},j-\frac{1}{2}} \\ E^{n+\frac{1}{2}}_{yc\ i,j+\frac{1}{2}} &\leftarrow E^{n-\frac{1}{2}}_{yc\ i,j+\frac{1}{2}},\ \textit{by using } H^{n}_{zc\ i+\frac{1}{2},j+\frac{1}{2}}, H^{n}_{zc\ i-\frac{1}{2},j+\frac{1}{2}} \end{aligned}$$

2. Update H_{zc} on the coarse mesh, from n to $n+1$.

$$H^{n+1}_{zc\ i+\frac{1}{2},j+\frac{1}{2}} \leftarrow H^{n}_{zc\ i+\frac{1}{2},j+\frac{1}{2}},\ \textit{by using } E^{n+\frac{1}{2}}_{xc\ i+\frac{1}{2},j+1}, E^{n+\frac{1}{2}}_{xc\ i+\frac{1}{2},j}, E^{n+\frac{1}{2}}_{yc\ i+1,j+\frac{1}{2}}, E^{n+\frac{1}{2}}_{yc\ i,j+\frac{1}{2}}$$

3. Interpolate electric field ghost value $\hat{E}^{n}_{xf}$ and $\hat{E}^{n}_{yf}$ using coarse mesh $E^{n-\frac{1}{2}}_{xc}$, $E^{n+\frac{1}{2}}_{xc}$, $E^{n-\frac{1}{2}}_{yc}$ and $E^{n+\frac{1}{2}}_{yc}$, respectively.

4. Update E_{xf} and E_{yf} on the fine mesh, from $n-\frac{1}{2}$ to n.

$$\begin{aligned} E^{n}_{xf\ i+\frac{1}{2},j} &\leftarrow E^{n-\frac{1}{2}}_{xf\ i+\frac{1}{2},j},\ \textit{by using } H^{n-\frac{1}{4}}_{zf\ i+\frac{1}{2},j+\frac{1}{2}}, H^{n-\frac{1}{4}}_{zf\ i+\frac{1}{2},j-\frac{1}{2}} \\ E^{n}_{yf\ i,j+\frac{1}{2}} &\leftarrow E^{n-\frac{1}{2}}_{yf\ i,j+\frac{1}{2}},\ \textit{by using } H^{n-\frac{1}{4}}_{zf\ i+\frac{1}{2},j+\frac{1}{2}}, H^{n-\frac{1}{4}}_{zf\ i-\frac{1}{2},j+\frac{1}{2}} \end{aligned}$$

5. Update H_{zf} on the fine mesh, from $n-\frac{1}{4}$ to $n+\frac{1}{4}$.

$$H^{n+\frac{1}{4}}_{zf\ i+\frac{1}{2},j+\frac{1}{2}} \leftarrow H^{n-\frac{1}{4}}_{zf\ i+\frac{1}{2},j+\frac{1}{2}},\ by\ using\ E^{n}_{xf\ i+\frac{1}{2},j+1}, E^{n}_{xf\ i+\frac{1}{2},j}, E^{n}_{yf\ i+1,j+\frac{1}{2}}, E^{n}_{yf\ i,j+\frac{1}{2}}$$

6. Interpolate electric field ghost value $\hat{E}^{n+\frac{1}{2}}_{xf}$ and $\hat{E}^{n+\frac{1}{2}}_{yf}$ using coarse mesh $E^{n+\frac{1}{2}}_{xc}$ and $E^{n+\frac{1}{2}}_{yc}$, respectively.

7. Update E_{xf} and E_{yf} on the fine mesh, from n to $n+\frac{1}{2}$.

$$E^{n+\frac{1}{2}}_{xf\ i+\frac{1}{2},j} \leftarrow E^{n}_{xf\ i+\frac{1}{2},j},\ by\ using\ H^{n+\frac{1}{4}}_{zf\ i+\frac{1}{2},j+\frac{1}{2}}, H^{n+\frac{1}{4}}_{zf\ i+\frac{1}{2},j-\frac{1}{2}}$$
$$E^{n+\frac{1}{2}}_{yf\ i,j+\frac{1}{2}} \leftarrow E^{n}_{yf\ i,j+\frac{1}{2}},\ by\ using\ H^{n+\frac{1}{4}}_{zf\ i+\frac{1}{2},j+\frac{1}{2}}, H^{n+\frac{1}{4}}_{zf\ i-\frac{1}{2},j+\frac{1}{2}}$$

8. Update H_{zf} on the fine mesh, from $n+\frac{1}{4}$ to $n+\frac{3}{4}$.

$$H^{n+\frac{3}{4}}_{zf\ i+\frac{1}{2},j+\frac{1}{2}} \leftarrow H^{n+\frac{1}{4}}_{zf\ i+\frac{1}{2},j+\frac{1}{2}},\ by\ using\ E^{n+\frac{1}{2}}_{xf\ i+\frac{1}{2},j+1}, E^{n+\frac{1}{2}}_{xf\ i+\frac{1}{2},j}, E^{n+\frac{1}{2}}_{yf\ i+1,j+\frac{1}{2}}, E^{n+\frac{1}{2}}_{yf\ i,j+\frac{1}{2}}$$

9. Replace E_{xc} and E_{yc} electric field by E_{xf} and E_{yf} in the region where fine grid overlaps coarse grid:

$$E^{n+\frac{1}{2}}_{xc\ i+\frac{1}{2},j} = E^{n+\frac{1}{2}}_{xf\ i+\frac{1}{2},j},$$

$$E^{n+\frac{1}{2}}_{yc\ i,j+\frac{1}{2}} = E^{n+\frac{1}{2}}_{yf\ i,j+\frac{1}{2}}.$$

10. Update H_{zc} on the coarse mesh as in step 2.

The above steps are applied recursively at each refinement level. In this case, the coarse grid E_{xc} and E_{yc} fields are updated once from time $n-1/2$ to $n+1/2$, followed by H_{zc} field update from time n to $n+1$. The fine mesh solutions are updated as follows: fields E_{xf} and E_{yf} are update from $n-1/2$ to n, followed by H_{zf} update from $n-1/4$ to $n+1/4$, then E_{xf} and E_{yf} update from n to $n+1/2$, followed by H_{zf} update from $n+1/4$ to $n+3/4$. In step 9, we replace the electric field on the coarse grid by the time averaged electric fields on the fine grid at the coarse/fine mesh

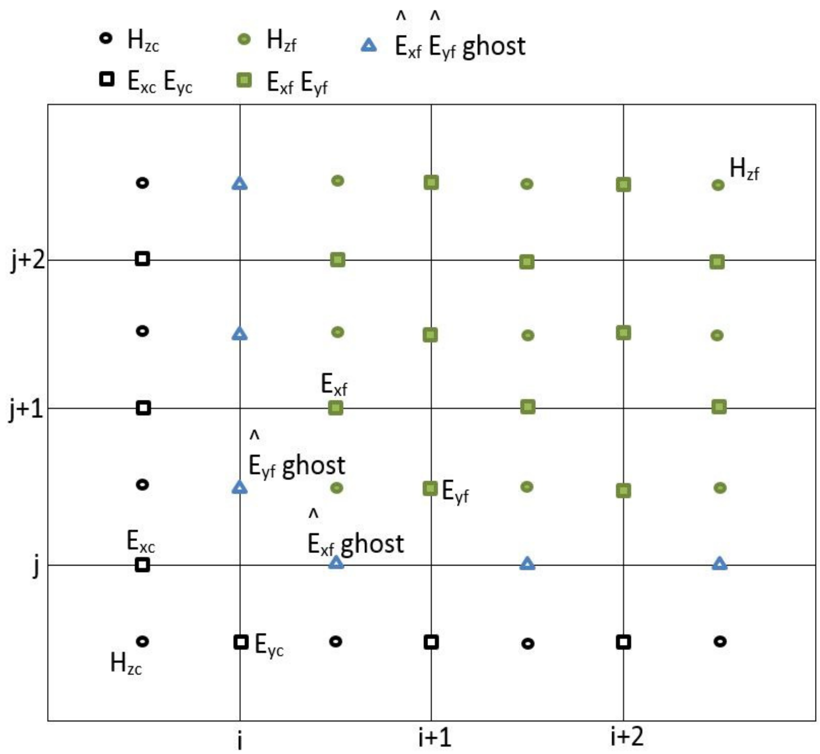

Figure 2.6: The temporal subcycling with GE for TE_z mode. Blue triangles denote the electric ghost values on the fine mesh boundary.

interface. The last step is to update magnetic filed by using the new electric filed values from step 9 on the coarse mesh.

In step 3, we interpolate electric field ghost value from coarse mesh:

$$\hat{E}^{n}_{xf\ i+\frac{1}{2},j} = \frac{1}{2}(E^{n-\frac{1}{2}}_{xc\ i+\frac{1}{2},j} + E^{n+\frac{1}{2}}_{xc\ i+\frac{1}{2},j}), \tag{2.21}$$

$$\hat{E}^{n}_{yf\ i,j+\frac{1}{2}} = \frac{1}{2}(E^{n-\frac{1}{2}}_{yc\ i,j+\frac{1}{2}} + E^{n+\frac{1}{2}}_{yc\ i,j+\frac{1}{2}}). \tag{2.22}$$

Similary, in step 6, we interpolate electric field ghost value from coarse mesh:

$$\hat{E}^{n+\frac{1}{2}}_{xf\ i+\frac{1}{2},j} = E^{n+\frac{1}{2}}_{xc\ i+\frac{1}{2},j}, \tag{2.23}$$

$$\hat{E}^{n+\frac{1}{2}}_{yf\ i,j+\frac{1}{2}} = E^{n+\frac{1}{2}}_{yc\ i,j+\frac{1}{2}}. \tag{2.24}$$

Chapter 3
THE ITERATION BASED TEMPORAL SUBCYCLING FDTD METHOD

3.1 Iteration Based Temporal Subcycling FDTD Method

In this section, we propose a novel iteration based temporal subcycling FDTD algorithm, focusing on overcoming the late-time instability problem of the conventional temporal subcycling FDTD method. The conventional temporal subcycling with coarse/fine mesh ratio 2:1 consists of the update of solution on coarse mesh by Δt time step and two consecutive $\Delta t/2$ updates of the fine mesh solutions, as shown in the flowchart in Figure 3.1(a). The basic idea of the iteration based subcycling technique is illustrated in the flowchat in Figure 3.1(b). After the first update on the fine mesh, due to the staggered nature of the electric and magnetic fields in Yee algorithm, the solutions on the coarse mesh can be recalculated using the fine mesh solutions before and after the first update.

The iteration based subcycling FDTD algorithm is summarized in the following steps:

1. Update E_{xc} and E_{yc} on the coarse mesh, from $n-\frac{1}{2}$ to $n+\frac{1}{2}$.

$$E^{n+\frac{1}{2}}_{xc\,i+\frac{1}{2},j} \leftarrow E^{n-\frac{1}{2}}_{xc\,i+\frac{1}{2},j},\ by\ using\ H^{n}_{zc\,i+\frac{1}{2},j+\frac{1}{2}}, H^{n}_{zc\,i+\frac{1}{2},j-\frac{1}{2}}$$
$$E^{n+\frac{1}{2}}_{yc\,i,j+\frac{1}{2}} \leftarrow E^{n-\frac{1}{2}}_{yc\,i,j+\frac{1}{2}},\ by\ using\ H^{n}_{zc\,i+\frac{1}{2},j+\frac{1}{2}}, H^{n}_{zc\,i-\frac{1}{2},j+\frac{1}{2}}$$

2. Update H_{zc} on the coarse mesh, from n to $n+1$.

$$H^{n+1}_{zc\,i+\frac{1}{2},j+\frac{1}{2}} \leftarrow H^{n}_{zc\,i+\frac{1}{2},j+\frac{1}{2}},\ by\ using\ E^{n+\frac{1}{2}}_{xc\,i+\frac{1}{2},j+1}, E^{n+\frac{1}{2}}_{xc\,i+\frac{1}{2},j}, E^{n+\frac{1}{2}}_{yc\,i+1,j+\frac{1}{2}}, E^{n+\frac{1}{2}}_{yc\,i,j+\frac{1}{2}}$$

3. Interpolate electric field ghost value $\hat{E}^{n}_{xf}$ and $\hat{E}^{n}_{yf}$ using the corresponding values on the coarse mesh $E^{n-\frac{1}{2}}_{xc}$, $E^{n+\frac{1}{2}}_{xc}$, $E^{n-\frac{1}{2}}_{yc}$ and $E^{n+\frac{1}{2}}_{yc}$.

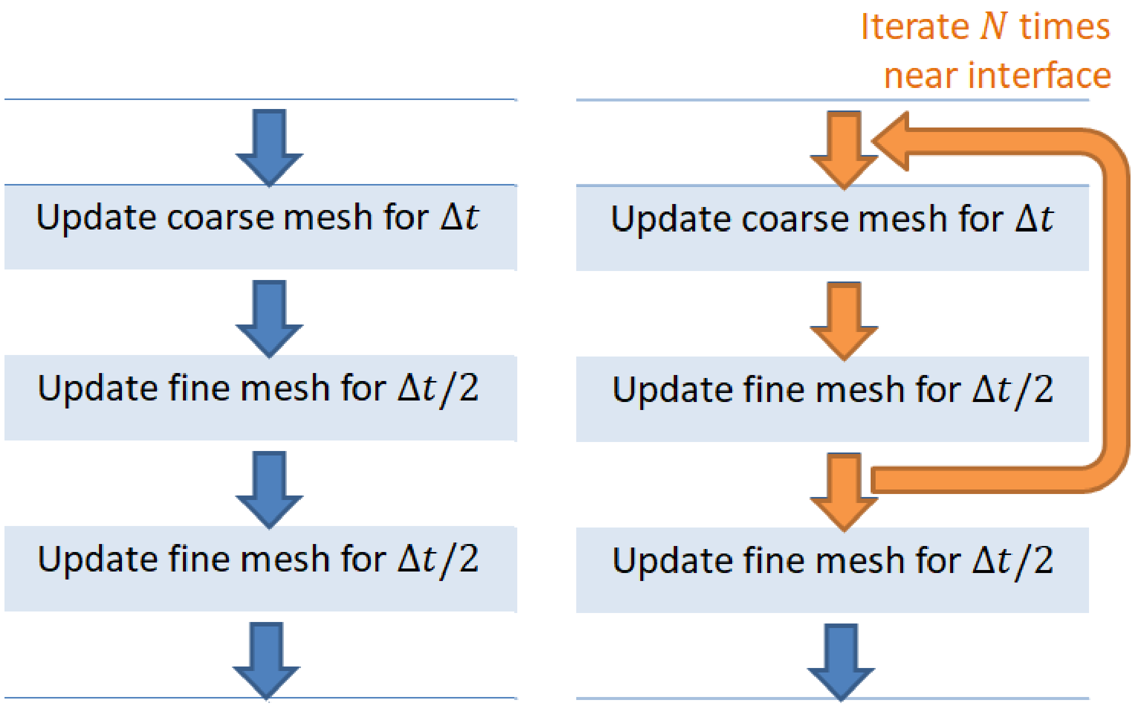

(a) (b)

Figure 3.1: Flowchart of (a) conventional and (b) iteration based temporal subcycling FDTD method.

4. Update E_{xf} and E_{yf} on the fine mesh, from $n-\frac{1}{2}$ to n.

$$E^{n}_{xf\ i+\frac{1}{2},j} \leftarrow E^{n-\frac{1}{2}}_{xf\ i+\frac{1}{2},j},\ by\ using\ H^{n-\frac{1}{4}}_{zf\ i+\frac{1}{2},j+\frac{1}{2}}, H^{n-\frac{1}{4}}_{zf\ i+\frac{1}{2},j-\frac{1}{2}}$$

$$E^{n}_{yf\ i,j+\frac{1}{2}} \leftarrow E^{n-\frac{1}{2}}_{yf\ i,j+\frac{1}{2}},\ by\ using\ H^{n-\frac{1}{4}}_{zf\ i+\frac{1}{2},j+\frac{1}{2}}, H^{n-\frac{1}{4}}_{zf\ i-\frac{1}{2},j+\frac{1}{2}}$$

5. Update H_{zf} on the fine mesh, from $n-\frac{1}{4}$ to $n+\frac{1}{4}$.

$$H^{n+\frac{1}{4}}_{zf\ i+\frac{1}{2},j+\frac{1}{2}} \leftarrow H^{n-\frac{1}{4}}_{zf\ i+\frac{1}{2},j+\frac{1}{2}},\ by\ using\ E^{n}_{xf\ i+\frac{1}{2},j+1}, E^{n}_{xf\ i+\frac{1}{2},j}, E^{n}_{yf\ i+1,j+\frac{1}{2}}, E^{n}_{yf\ i,j+\frac{1}{2}}$$

6. Recalculate the coarse grid H_{zc} values on the coarse/fine mesh interface at time step n using

the fine mesh values H_{zf} at time levels $n-\frac{1}{4}$ and $n+\frac{1}{4}$.

$$H^{n}_{zc\,i+\frac{1}{2},j+\frac{1}{2}} = \frac{1}{2}(H^{n-\frac{1}{4}}_{zf\,i+\frac{1}{2},j+\frac{1}{2}} + H^{n+\frac{1}{4}}_{zf\,i+\frac{1}{2},j+\frac{1}{2}}).$$

7. Repeat from step 1 to step 6 for N times for the solutions on the coarse/fine mesh interface.

8. Interpolate electric field ghost values $\hat{E}^{n+\frac{1}{2}}_{xf}$ and $\hat{E}^{n+\frac{1}{2}}_{yf}$ using the corresponding coarse mesh values $E^{n+\frac{1}{2}}_{xc}$ and $E^{n+\frac{1}{2}}_{yc}$.

9. Update E_{xf} and E_{yf} on the fine mesh, from n to $n+\frac{1}{2}$.

$$E^{n+\frac{1}{2}}_{xf\,i+\frac{1}{2},j} \leftarrow E^{n}_{xf\,i+\frac{1}{2},j},\ by\ using\ H^{n+\frac{1}{4}}_{zf\,i+\frac{1}{2},j+\frac{1}{2}}, H^{n+\frac{1}{4}}_{zf\,i+\frac{1}{2},j-\frac{1}{2}}$$
$$E^{n+\frac{1}{2}}_{yf\,i,j+\frac{1}{2}} \leftarrow E^{n}_{yf\,i,j+\frac{1}{2}},\ by\ using\ H^{n+\frac{1}{4}}_{zf\,i+\frac{1}{2},j+\frac{1}{2}}, H^{n+\frac{1}{4}}_{zf\,i-\frac{1}{2},j+\frac{1}{2}}$$

10. Update H_{zf} on the fine mesh, from $n+\frac{1}{4}$ to $n+\frac{3}{4}$.

$$H^{n+\frac{3}{4}}_{zf\,i+\frac{1}{2},j+\frac{1}{2}} \leftarrow H^{n+\frac{1}{4}}_{zf\,i+\frac{1}{2},j+\frac{1}{2}},\ by\ using\ E^{n+\frac{1}{2}}_{xf\,i+\frac{1}{2},j+1}, E^{n+\frac{1}{2}}_{xf\,i+\frac{1}{2},j}, E^{n+\frac{1}{2}}_{yf\,i+1,j+\frac{1}{2}}, E^{n+\frac{1}{2}}_{yf\,i,j+\frac{1}{2}}$$

11. Replace the coarse grid electric fields E_{xc} and E_{yc} by the corresponding fine grid values E_{xf} and E_{yf} in the region where fine grid overlaps coarse grid:

$$E^{n+\frac{1}{2}}_{xc\,i+\frac{1}{2},j} = E^{n+\frac{1}{2}}_{xf\,i+\frac{1}{2},j},$$

$$E^{n+\frac{1}{2}}_{yc\,i,j+\frac{1}{2}} = E^{n+\frac{1}{2}}_{yf\,i,j+\frac{1}{2}}.$$

12. Redo the update of H_{zc} on the coarse mesh as in step 2.

A key step of the iteration based time subcycling algorithm is the step 7 where the iteration is carried out for N times. Through eigenvalue tests, we found that $N \geq 4$ guarantees the stability where the amplification factor (the largest eigenvalue of the update equations) is 1. To compare with the GE subcycling method in section 2.4.2, we add the step 6 and step 7 to repetitive update the coarse magnetic filed values H_{zc} at time n by using fine mesh magnetic field values H_{zf} at time step $n-1/4$ and $n+1/4$. This is because we compute the fine mesh E_{xf} and E_{yf} in the subgrid from time step $n-1/2$ to n and fine mesh H_{zf} from time step $n-1/4$ to $n+1/4$. At this point, we can average the fine mesh H_{zf} at time step $n-1/4$ and $n+1/4$ to replace coarse mesh H_{zc} at time step n (step 6). The new coarse mesh magnetic field values H_{zc} at time step n will be used to update the coarse mesh electric field values E_{xc} and E_{yc} from time step $n-1/2$ to $n+1/2$ again as in the step 1. Thus, the coarse grid magnetic and electric fields are updated. Then in the step 3, electric field is interpolated again to get the new ghost cell values. Therefore, the fine region values can be updated again from the new ghost values and magnetic field values at the interface. The step 12 is to update magnetic filed by using the new electric filed values from step 11 in the coarse region.

3.2 Iteration Based Temporal Subcycling and Spatial Subgridding FDTD Method

In this section, the spatial subgridding and temporal subcycling method are combined to obtain the best efficiency and accuracy. The region using the subcycling method is overlapping and larger than the region using the spatial subgridding method. In this section, we use the proposed iteration based temporal subcycling algorithm and spatial subgridding algorithm that proposed in section 2.3.2 (The spatial subgridding with GHF method). We refer our method the Iteration Based Subgridding (IBS) FDTD algorithm. Let region A be the region with temporal subcycling and region B be the region with spatial subgridding. The distance between the fine region A and B is chosen to be 2 cells. The combined temporal subcycling and spatial subgridding method (IBS-FDTD) is summarized in the following steps,

1. Update E_{xc} and E_{yc} on the coarse mesh, from $n-\frac{1}{2}$ to $n+\frac{1}{2}$.

$$E^{n+\frac{1}{2}}_{xc\ i+\frac{1}{2},j} \leftarrow E^{n-\frac{1}{2}}_{xc\ i+\frac{1}{2},j},\ by\ using\ H^{n}_{zc\ i+\frac{1}{2},j+\frac{1}{2}}, H^{n}_{zc\ i+\frac{1}{2},j-\frac{1}{2}}$$
$$E^{n+\frac{1}{2}}_{yc\ i,j+\frac{1}{2}} \leftarrow E^{n-\frac{1}{2}}_{yc\ i,j+\frac{1}{2}},\ by\ using\ H^{n}_{zc\ i+\frac{1}{2},j+\frac{1}{2}}, H^{n}_{zc\ i-\frac{1}{2},j+\frac{1}{2}}$$

2. Update H_{zc} on the coarse mesh, from n to $n+1$.

$$H^{n+1}_{zc\ i+\frac{1}{2},j+\frac{1}{2}} \leftarrow H^{n}_{zc\ i+\frac{1}{2},j+\frac{1}{2}},\ by\ using\ E^{n+\frac{1}{2}}_{xc\ i+\frac{1}{2},j+1}, E^{n+\frac{1}{2}}_{xc\ i+\frac{1}{2},j}, E^{n+\frac{1}{2}}_{yc\ i+1,j+\frac{1}{2}}, E^{n+\frac{1}{2}}_{yc\ i,j+\frac{1}{2}}$$

3. Interpolate electric field ghost value $\hat{E}^{n}_{xf}$ and $\hat{E}^{n}_{yf}$ using corresponding coarse mesh values $E^{n-\frac{1}{2}}_{xc}$, $E^{n+\frac{1}{2}}_{xc}$, $E^{n-\frac{1}{2}}_{yc}$ and $E^{n+\frac{1}{2}}_{yc}$.

4. Update E_{xf} and E_{yf} on the temporal fine mesh, from $n-\frac{1}{2}$ to n.

$$E^{n}_{xf\ i+\frac{1}{2},j} \leftarrow E^{n-\frac{1}{2}}_{xf\ i+\frac{1}{2},j},\ by\ using\ H^{n-\frac{1}{4}}_{zf\ i+\frac{1}{2},j+\frac{1}{2}}, H^{n-\frac{1}{4}}_{zf\ i+\frac{1}{2},j-\frac{1}{2}}$$
$$E^{n}_{yf\ i,j+\frac{1}{2}} \leftarrow E^{n-\frac{1}{2}}_{yf\ i,j+\frac{1}{2}},\ by\ using\ H^{n-\frac{1}{4}}_{zf\ i+\frac{1}{2},j+\frac{1}{2}}, H^{n-\frac{1}{4}}_{zf\ i-\frac{1}{2},j+\frac{1}{2}}$$

5. Update H_{zf} on the temporal fine mesh, from $n-\frac{1}{4}$ to $n+\frac{1}{4}$.

$$H^{n+\frac{1}{4}}_{zf\ i+\frac{1}{2},j+\frac{1}{2}} \leftarrow H^{n-\frac{1}{4}}_{zf\ i+\frac{1}{2},j+\frac{1}{2}},\ by\ using\ E^{n}_{xf\ i+\frac{1}{2},j+1}, E^{n}_{xf\ i+\frac{1}{2},j}, E^{n}_{yf\ i+1,j+\frac{1}{2}}, E^{n}_{yf\ i,j+\frac{1}{2}}$$

6. Recalculate the coarse grid H_{zc} values on the coarse/temporal fine mesh interface at time step n using the fine mesh values H_{zf} at time levels $n-\frac{1}{4}$ and $n+\frac{1}{4}$.

$$H^{n}_{zc\ i+\frac{1}{2},j+\frac{1}{2}} = \frac{1}{2}(H^{n-\frac{1}{4}}_{zf\ i+\frac{1}{2},j+\frac{1}{2}} + H^{n+\frac{1}{4}}_{zf\ i+\frac{1}{2},j+\frac{1}{2}}).$$

7. Repeat from step 1 to step 6 for N times for the solutions on the coarse/temporal fine mesh interface.

8. Interpolate magnetic field ghost values $\hat{H}_{fz\ i+\frac{1}{4},j+\frac{1}{4}}$, $\hat{H}_{fz\ i+\frac{3}{4},j+\frac{1}{4}}$ and $\hat{H}_{fz\ i+\frac{1}{4},j+\frac{3}{4}}$ using corresponding temporal fine mesh values $H_{zf\ i-\frac{1}{2},j-\frac{1}{2}}$, $H_{zf\ i+\frac{1}{2},j-\frac{1}{2}}$, $H_{zf\ i-\frac{1}{2},j+\frac{1}{2}}$, $H_{zf\ i+\frac{1}{2},j+\frac{1}{2}}$, $H_{zf\ i+\frac{3}{2},j-\frac{1}{2}}$, $H_{zf\ i+\frac{3}{2},j+\frac{1}{2}}$, $H_{zf\ i-\frac{1}{2},j+\frac{3}{2}}$ and $H_{zf\ i+\frac{1}{2},j+\frac{3}{2}}$ at time $n+\frac{1}{4}$.

9. Update H_{fz} on the spatial fine mesh, from $n-\frac{1}{4}$ to $n+\frac{1}{4}$.

$$H^{n+\frac{1}{4}}_{fz\ i+\frac{3}{4},j+\frac{3}{4}} \leftarrow H^{n-\frac{1}{4}}_{fz\ i+\frac{3}{4},j+\frac{3}{4}},\ by\ using\ E^{n}_{fx\ i+\frac{3}{4},j+\frac{1}{2}}, E^{n}_{fx\ i+\frac{3}{4},j+1}, E^{n}_{fy\ i+\frac{1}{2},j+\frac{3}{4}}, E^{n}_{fy\ i+1,j+\frac{3}{4}}$$

10. Update E_{fx} and E_{fy} on the spatial fine mesh, from n to $n+\frac{1}{2}$.

$$E^{n+\frac{1}{2}}_{fx\ i+\frac{3}{4},j+\frac{1}{2}} \leftarrow E^{n}_{fx\ i+\frac{3}{4},j+\frac{1}{2}},\ by\ using\ H^{n+\frac{1}{4}}_{fz\ i+\frac{3}{4},j+\frac{3}{4}}, H^{n+\frac{1}{4}}_{fz\ i+\frac{3}{4},j+\frac{1}{4}}$$
$$E^{n+\frac{1}{2}}_{fy\ i+\frac{1}{2},j+\frac{3}{4}} \leftarrow E^{n}_{fy\ i+\frac{1}{2},j+\frac{3}{4}},\ by\ using\ H^{n+\frac{1}{4}}_{fz\ i+\frac{3}{4},j+\frac{3}{4}}, H^{n+\frac{1}{4}}_{fz\ i+\frac{1}{4},j+\frac{3}{4}}$$

11. Replace H_{zf} magnetic field by H_{fz} in the region where spatial fine grid B overlaps temporal fine grid A:

$$H^{n+\frac{1}{4}}_{zf\ i+\frac{1}{2},j+\frac{1}{2}} = \frac{1}{4}(H^{n+\frac{1}{4}}_{fz\ i+\frac{1}{4},j+\frac{1}{4}} + H^{n+\frac{1}{4}}_{fz\ i+\frac{3}{4},j+\frac{1}{4}} + H^{n+\frac{1}{4}}_{fz\ i+\frac{1}{4},j+\frac{3}{4}} + H^{n+\frac{1}{4}}_{fz\ i+\frac{3}{4},j+\frac{3}{4}}).$$

12. Interpolate electric field ghost value $\hat{E}^{n+\frac{1}{2}}_{xf}$ and $\hat{E}^{n+\frac{1}{2}}_{yf}$ using corresponding coarse mesh values $E^{n+\frac{1}{2}}_{xc}$ and $E^{n+\frac{1}{2}}_{yc}$.

13. Update E_{xf} and E_{yf} on the temporal fine mesh, from n to $n+\frac{1}{2}$.

$$E^{n+\frac{1}{2}}_{xf\ i+\frac{1}{2},j} \leftarrow E^{n}_{xf\ i+\frac{1}{2},j},\ by\ using\ H^{n+\frac{1}{4}}_{zf\ i+\frac{1}{2},j+\frac{1}{2}}, H^{n+\frac{1}{4}}_{zf\ i+\frac{1}{2},j-\frac{1}{2}}$$
$$E^{n+\frac{1}{2}}_{yf\ i,j+\frac{1}{2}} \leftarrow E^{n}_{yf\ i,j+\frac{1}{2}},\ by\ using\ H^{n+\frac{1}{4}}_{zf\ i+\frac{1}{2},j+\frac{1}{2}}, H^{n+\frac{1}{4}}_{zf\ i-\frac{1}{2},j+\frac{1}{2}}$$

14. Update H_{zf} on the temporal fine mesh, from $n+\frac{1}{4}$ to $n+\frac{3}{4}$.

$$H^{n+\frac{3}{4}}_{zf\ i+\frac{1}{2},j+\frac{1}{2}} \leftarrow H^{n+\frac{1}{4}}_{zf\ i+\frac{1}{2},j+\frac{1}{2}},\ by\ using\ E^{n+\frac{1}{2}}_{xf\ i+\frac{1}{2},j+1}, E^{n+\frac{1}{2}}_{xf\ i+\frac{1}{2},j}, E^{n+\frac{1}{2}}_{yf\ i+1,j+\frac{1}{2}}, E^{n+\frac{1}{2}}_{yf\ i,j+\frac{1}{2}}$$

15. Interpolate magnetic field ghost values $\hat{H}_{fz\ i+\frac{1}{4},j+\frac{1}{4}}$, $\hat{H}_{fz\ i+\frac{3}{4},j+\frac{1}{4}}$ and $\hat{H}_{fz\ i+\frac{1}{4},j+\frac{3}{4}}$ using corresponding temporal fine mesh values $H_{zf\ i-\frac{1}{2},j-\frac{1}{2}}$, $H_{zf\ i+\frac{1}{2},j-\frac{1}{2}}$, $H_{zf\ i-\frac{1}{2},j+\frac{1}{2}}$, $H_{zf\ i+\frac{1}{2},j+\frac{1}{2}}$, $H_{zf\ i+\frac{3}{2},j-\frac{1}{2}}$, $H_{zf\ i+\frac{3}{2},j+\frac{1}{2}}$, $H_{zf\ i-\frac{1}{2},j+\frac{3}{2}}$ and $H_{zf\ i+\frac{1}{2},j+\frac{3}{2}}$ at time $n+\frac{3}{4}$.

16. Update H_{fz} on the spatial fine mesh, from $n+\frac{1}{4}$ to $n+\frac{3}{4}$.

$$H^{n+\frac{3}{4}}_{fz\ i+\frac{3}{4},j+\frac{3}{4}} \leftarrow H^{n+\frac{1}{4}}_{fz\ i+\frac{3}{4},j+\frac{3}{4}},\ by\ using\ E^{n+\frac{1}{2}}_{fx\ i+\frac{3}{4},j+\frac{1}{2}}, E^{n+\frac{1}{2}}_{fx\ i+\frac{3}{4},j+1}, E^{n+\frac{1}{2}}_{fy\ i+\frac{1}{2},j+\frac{3}{4}}, E^{n+\frac{1}{2}}_{fy\ i+1,j+\frac{3}{4}}$$

17. Update E_{fx} and E_{fy} on the spatial fine mesh, from $n+\frac{1}{2}$ to $n+1$.

$$E^{n+1}_{fx\ i+\frac{3}{4},j+\frac{1}{2}} \leftarrow E^{n+\frac{1}{2}}_{fx\ i+\frac{3}{4},j+\frac{1}{2}},\ by\ using\ H^{n+\frac{3}{4}}_{fz\ i+\frac{3}{4},j+\frac{3}{4}}, H^{n+\frac{3}{4}}_{fz\ i+\frac{3}{4},j+\frac{1}{4}}$$
$$E^{n+1}_{fy\ i+\frac{1}{2},j+\frac{3}{4}} \leftarrow E^{n+\frac{1}{2}}_{fy\ i+\frac{1}{2},j+\frac{3}{4}},\ by\ using\ H^{n+\frac{3}{4}}_{fz\ i+\frac{3}{4},j+\frac{3}{4}}, H^{n+\frac{3}{4}}_{fz\ i+\frac{1}{4},j+\frac{3}{4}}$$

18. Replace H_{zf} magnetic field by H_{fz} in the region where spatial fine grid B overlaps temporal fine grid A:

$$H^{n+\frac{3}{4}}_{zf\ i+\frac{1}{2},j+\frac{1}{2}} = \frac{1}{4}(H^{n+\frac{3}{4}}_{fz\ i+\frac{1}{4},j+\frac{1}{4}} + H^{n+\frac{3}{4}}_{fz\ i+\frac{3}{4},j+\frac{1}{4}} + H^{n+\frac{3}{4}}_{fz\ i+\frac{1}{4},j+\frac{3}{4}} + H^{n+\frac{3}{4}}_{fz\ i+\frac{3}{4},j+\frac{3}{4}}).$$

19. Replace H_{zc} magnetic field by H_{zf} in the region where temporal fine grid A overlaps coarse grid:

$$H^{n+1}_{zc\ i+\frac{1}{2},j+\frac{1}{2}} = H^{n+\frac{3}{4}}_{zf\ i+\frac{1}{2},j+\frac{1}{2}}.$$

20. Redo the update of E_{xc} and E_{yc} on the coarse mesh as in step 1.

In the above algorithm, we assume that electric field and magnetic field are denoted by E_{xc}, E_{yc} and H_{zc} in the coarse region, E_{xf}, E_{yf} and H_{zf} in the temporal fine region A and E_{fx}, E_{fy} and H_{fz} in the spatial fine region B. Firstly, we update the coarse mesh E_{xc} and E_{yc} from time step $n-1/2$ to $n+1/2$ and H_{zc} from time step n to $n+1$. Then, we need to use the electric field value in coarse mesh to compute the electric field ghost boundary value in the temporal fine region A at n.

We use the ghost boundary value to update E_{xf} and E_{yf} from time step $n-1/2$ to n and H_{zf} from time step $n-1/4$ to $n+1/4$. After that we do the N times iteration from step 1 to step 6. Then, we use the magnetic filed value in the temporal fine region A to compute the magnetic field ghost boundary value in the spatial fine region B at $n+1/4$. In step 9 and step 10, we update the electric field E_{fx} and E_{fy} from time step n to $n+1/2$ and magnetic field H_{fz} from time step $n-1/4$ to $n+1/4$ in the spatial fine region B. We replace the H_{zf} by averaging the H_{fz} in the region where spatial fine region B overlaps temporal fine region A at $n+1/4$. Next we use the electric field value in coarse mesh to compute the electric field ghost boundary value in the temporal fine region A at $n+1/2$. Then we update E_{xf} and E_{yf} from time step n to $n+1/2$ and H_{zf} from time step $n+1/4$ to $n+3/4$. At $n+1/4$ to calculate the magnetic ghost boundary value in the region B using the magnetic filed H_{zf}. Thus, update the electric field E_{fx} and E_{fy} from time step $n+1/2$ to $n+1$ and magnetic field H_{fz} from time step $n+1/4$ to $n+3/4$ in the spatial fine region B. Similar to step 11, we average the H_{fz} to replace the H_{zf} at time step $n+3/4$. Finally, we replace the magnetic field H_{zc} with the corresponding H_{zf} and then update electric filed E_{xc} and E_{yc} as step 1.

Chapter 4
THROUGH-THE-WALL RADAR DETECTION ANALYSIS

4.1 Radar Basic Model

A basic principle of the through-the-wall radar is shown in Figure 4.1. Through-the-wall radar generates and transmits a short pulse through the transmitting antenna TX. The signal propagates in an environment. When it meets target, part of the electromagnetic energy is reflected from the object and propagates back to receiving antenna RX, then the receiving antenna records the reflected return signal.

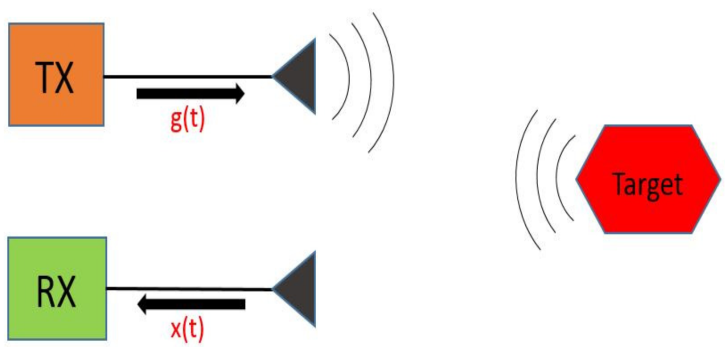

Figure 4.1: Basic principle of the through-the-wall radar.

Most imaging radar systems make use of the $start - stop$ approximation [17], in which the sensor and scattering object are assumed to be stationary during the propagation. Assume that the region between the sensors and the scattering objects consists of a homogeneous, lossless, non-dispersive atmosphere, then in this situation, Maxwell's equations [23] can be used to obtain an homogeneous wave equation for the electromagnetic field as:

$$(\nabla^2 - \frac{1}{c^2}\frac{\partial^2}{\partial t^2})u(t,x) = s(t,x). \tag{4.1}$$

The fundamental solution [47] of the wave equation (4.1) is

$$u(t,x) = -\int g(t-t',x-y)s(t',y)dt'dy, \tag{4.2}$$

where $g(t,x)$ is the Green's function [39]

$$g(t,x) = \frac{\delta(t-|x|/c)}{4\pi|x|}. \tag{4.3}$$

For radar imaging, the field u includes two terms: $u = u^{in} + u^{sc}$, where the incident field u^{in} models the transmitting wave and the scatter field u^{sc} models the scattering wave. For stationary objects consisting of linear materials, we can write our scalar model as

$$u^{sc}(t,x) = -\int \nu(t-t',x)u(t',x)dt', \tag{4.4}$$

where $\nu(t,x)$ is called the reflectivity function. Combining equations (4.1) and (4.4), the scatter field can be expressed as [31]

$$u^{sc}(t,x) = \int\int g(t-\tau,x-z)\int \nu(\tau-t',z)u(t',z)dt'd\tau dz. \tag{4.5}$$

We measure u^{sc} at the antenna, and we determine the reflectivity function ν from these measurements. The nonlinearity in equation (4.5) makes it difficult to solve for ν. Consequently, almost all work on radar imaging includes using the *Born approximation*, which is also known as the $weak-scattering$ or $single-scattering$ approximation [31, 26]. The Born approximation replaces u on the right-hand side of equation (4.5) by the incident field u^{in}. Assume the reflectivity function $\nu(t,x)$ is independent of the frequency of the field, corresponding to $\nu(t,x) = \delta(t)\sigma(t)$, the equation (4.5) corresponds to the following formula

$$u^{sc}(t,x_0) \approx \int\int g(t-\tau,x_0-z)\sigma(z)u^{in}(\tau,z)d\tau dz, \tag{4.6}$$

or

$$u^{sc}(t, x_0) = \int \frac{\sigma(z) u^{in}(t - X(z; x_0)/c)}{4\pi X(z; x_0)} dz, \tag{4.7}$$

where $u^{sc}(t; r_0)$ is the measured space-time data at the antenna position x_0, $X(z; x_0)$ is the total travel distance from the transmitting antenna to the target space point z and onto the receiver, $\sigma(z)$ is the reflection coefficient at the target space point r. In our radar situations, we use the common point-target model [20], in which the target scene is treated as a discrete grid, and the target is treated as point-target. By employing the common point-target model, the received measurement u^{sc} in the equation (4.7) can be simply written as

$$u^{sc} = \sum_{i=1}^{L} \sigma_i u^{in}(t - \tau_i). \tag{4.8}$$

where L is the number of scatters in the target space, τ_i is the total trip delay from the transmitting antenna to the scatter i and back to receiving antenna, and σ_i is the coefficient related to reflection of the scatter, attenuation and spreading losses through propagation. Thus, the received signal is essentially a delayed and scaled version of the transmitted pulse (Figure 4.2).

In this dissertation, we are considering the two-dimensional problem, assuming that our room is a rectangle of size L_x by L_y and the walls are of a uniform thickness h, with relative electric permittivity ϵ_w. In order to reduce the effect of the wall, the wall signal is also extracted and removed from the original signal. There are excellent references about all parameter estimation and wall signal removal [10, 25]. The object The object inside the room is a convex domain $O \subset [0, L_x] \times [0, L_y]$ that has uniform relative electric permittivity ϵ_0. To model the actual problem, we will record and use data that could be gathered from a set of antenna transmitters and receivers. Thus, for any given simulation, we will assume that the electromagnetic waves are generated from a set of transmitters (TX) positioned outside of the room and the data is recorded from a set of receivers (RX), also positioned outside the room.

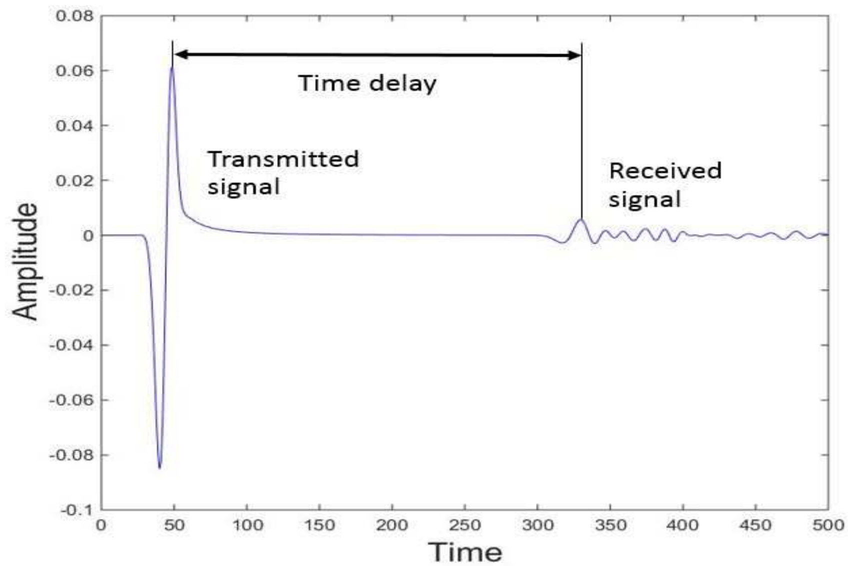

Figure 4.2: Signal delay of the through-the-wall radar.

4.2 Radar Imaging Method

In the previous sections, we have been discussing the method to detect where the objects and sources are, and calculate the total distance traveled by the wave that sent from the transmitter and meet the target back to the receiver. For this section, we introduce the inverse problem for through-the-wall radar imaging. We assume that the room is a rectangle of size L_x by L_y, and an object is inside this room. From the previous step data, we want to locate and reconstruct the object in the room. We will try two ways to set up the transmitters and receivers outside of the room. One of the ways is multiple transmitters and receivers on each side of the room, the other one is one transmitter and a finite number of receivers on each side of the room.

4.2.1 Target location detection

Due to the object inside the room, we know that the data on the receivers is difference from the data of an empty room. We can use the information from the forward problem to calculate the wave propagation in the empty room. The difference between the data gathered by the receivers

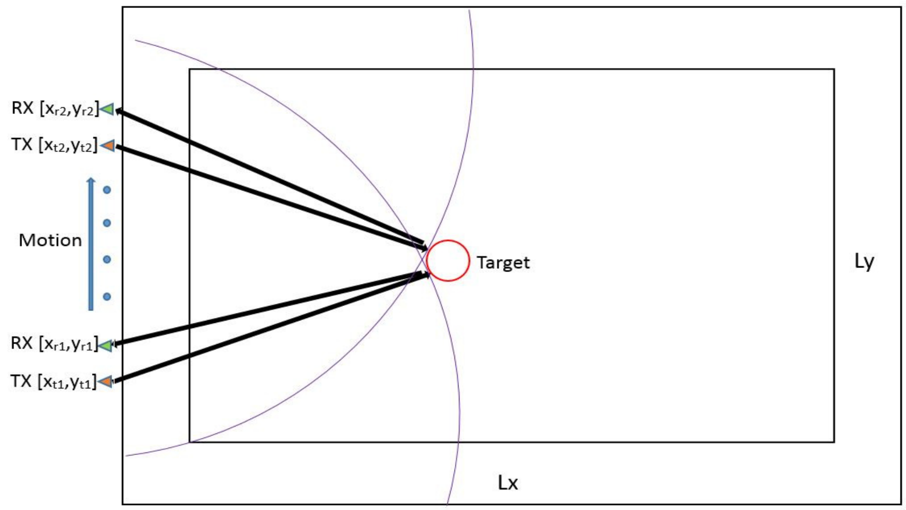

Figure 4.3: Illustration of the TWR procedure for multiple transmitters and receivers.

from an empty room and the room with object, we can determine the distance of the object from the transmitter and receiver. We assume that the wave equations have uniform speed of propagation and the wave front that hits the target and returns to the receiver travels in straight lines as shown in Figure 4.3. The black arrow lines show the actual path the wave traveled, and the red circle is the target inside the room. The orange triangles and the green triangles are represented the transmitters and receivers, respectively.

When the time delay T is obtained, the distance traveled is given by cT, where $c = \frac{1}{\sqrt{\epsilon_0 \mu_0}}$ is the speed of light in the room and $c = 2.998 \times 10^8 m/s$ in vacuum. The $\epsilon_0 = 8.854 \times 10^{-12} F/m$ is called electric permittivity of vacuum and $\mu_0 = 4\pi \times 10^{-7} H/m$ is called the magnetic permeability of vacuum. However, the wave also passes through a wall with a relative electric permittivity ϵ_w, so the wave speed is slower inside the wall and the time in this region needs to be calculated. We assume that the speed of the wave traveled inside the wall is denoted by $\frac{c}{\sqrt{\epsilon_w}}$. Thus, the total distance traveled by the wave can be represented as

$$d = t_r c + t_w \frac{c}{\sqrt{\epsilon_w}}. \tag{4.9}$$

where t_r denotes the time spent inside the room (in vacuum), and t_w is the time spent inside the wall. We can easily obtain that $t_r + t_w = T$. Because the wave passes through the wall twice, sending from the transmitter and returning to the receiver, the $t_w \approx 2h/(c/\sqrt{\epsilon_w})$ where h is the thickness of the wall. Since we don't know where the object is, we ignore the fact that the wave is going to pass through the wall at an angle.

We use the distance d to construct an ellipse with foci at the transmitter and receiver as the purple curve in Figure 4.3. The object must be externally tangent to the curve [11]. By creating these ellipses for each pair of transmitter/receiver data, we get an approximate outline as to where the object is.

4.2.2 Target characterization analysis

As we know the object location from the previous step, then we need to analyze the shape and size of the object. We use the method proposed in [11] to reconstruct the object starting with an initial guess of the center of the object.

To construct an ellipse with foci at the transmitter and receiver, we are going to use distance d and the properties of an ellipse. We assume that transmitter is at $F_1 = (x_t, y_t)$ and receiver is at $F_2 = (x_r, y_r)$ where F_1 and F_2 are the foci of the ellipse. Then, we can get the midpoint $C = (x_c, y_c)$ of the line segment joining the foci which is the center of the ellipse. For any point P on the ellipse, we know the sum of the distances $|PF_1|$, $|PF_2|$ to two fixed points F_1, F_2 the foci is usually denoted by $2a$ where a is called the semi major axis of the ellipse. Thus we have

$$|PF_1| + |PF_2| = 2a, \quad a > 0. \tag{4.10}$$

Since the ellipse must be externally tangent to the object, the point of tangency with the boundary of object is on the ellipse. d is the sum of the distance from the point of tangency to the transmitter TX and the receiver RX, then we get $a = \frac{1}{2}d$. The distance between the center of the ellipse C and the foci of ellipse F_1/F_2 is denoted by f. We calculate the semi minor axis of the ellipse b by using the equation $b^2 = a^2 - f^2$. Using the center of the object $O = (m, n)$ and the pervious data we have, we can find the point of tangency of the ellipse with the boundary of object on the ellipse using the bisection method [8]. Based on the forward information and the above main concept of the object reconstruction, the algorithm is summarized below:

1. Calculate the semi major axis a and semi minor axis b of the ellipse with foci at the transmitter TX and receiver RX, then find the center C of the ellipse.

2. Make a guess for the center of the object O. The initial guess is usually the center of the room.

3. Calculate the closest point P on each ellipse to the current center point guess by using bisection method.

4. Average the x and y coordinates of these closest points to get a new guess for the center point.

5. Repeat this procedure from step 3 until the center points converge to a value within a desired accuracy.

The most challenging part in this algorithm is step 3 about how to get the closest point on each ellipse to the center of the object. Assume our target is a convex object in the room, the closest point on each ellipse is the point of tangency of the ellipse with the boundary of the object. Then, we average the x and y coordinates of these closest points as the new center point of the object. In our cases, we define the ellipse in parametric form:

$$\begin{cases} x = a\cos\theta, \\ y = b\sin\theta. \end{cases} \tag{4.11}$$

where x and y are the coordinate of the point on the ellipse, a is the semi major axis and b is the semi minor axis of the ellipse, and θ is interpretations of parameter. The input for the bisection method is a continuous function $f(\theta)$ defined on an interval $[\theta_1, \theta_2]$ and the parameter $\theta \in [0, 2\pi]$ is called the eccentric anomaly, where $f(\theta_1)$ and $f(\theta_2)$ have opposite signs. Thus, we calculate the closest point used bisection method. By the intermediate value theorem, the continuous function

$f(\theta)$ must have at least one root in the current interval. The point of tangency is calculated using the root obtained from the previous step. The bisection method algorithm is given as follows:

Algorithm 1: The Bisection Method Algorithm

Input: Function f, endpoint values θ_1 and θ_2, tolerance TOL,
    `/*` $\theta_1 < \theta_2$`, either` $f(\theta_1) < 0$ `and` $f(\theta_2) > 0$ `or` $f(\theta_1) > 0$ `and` $f(\theta_2) < 0$ `*/`
Output: Value which differs from a root of function $f(\theta)$ by less than TOL
Set a is the semi major axis and b is the semi minor axis of the ellipse
while $|b - a| > TOL$ **do**
  $c = \frac{(a+b)}{2}$;
  if *sign of* $f(a)$=*sign of* $f(c)$ **then**
    $a = c$;
    else
      $b = c$;
  end
  $root = c$;
end

The iterative process defined above converges to a point inside the object, where the closest points on each ellipse are the tangency points. These closest points give a reasonable outline of the object, allowing us to see what the object looks like from this data. Whether or not we find the actual center of the object and how close we get to the boundary of object depends on the set of transmitters and receivers. For example, if there is no data from the top side of the object, this method will not move the center point closer to the top side. This may result in skewed shapes, so in comparison, the system works better if there is data from all sides.

As shown in the numerical examples, this procedure gives us results fairly close to the actual center point of the object, as well as a decent outline of the object, providing an approximation to its shape.

Chapter 5
NUMERICAL EXAMPLES

In this chapter, we first show the numerical results to analyze the accuracy and stability of the standard spatial subgridding and temporal subcycling method in 2D case. We then implement the proposed iteration based temporal subcycling method. The numerical examples are presented to test the new algorithm. Finally, we apply the our method to the through-the-wall radar simulations and compare it with the standard FDTD result.

5.1 Numerical Examples for Spatial Subgridding Method

In this section, we show numerical results of the spatial subgridding FDTD method in 2D. The ratio of the coarse and fine regions is 1:2 (in space). In the first example, we study the solution of a cylindrical wave in free space. The incidence source of a sine wave with wavelength $0.05\mu m$ is placed in the center of the domain.

$$H_{zc}(N_x, N_y) = \sin((2\pi c n \Delta t)/\lambda),$$

where $(N_x, N_y) = (200, 200)$ located at the center of the computation domain. The computational grid size is 400×400 with PML boundaries in x and y directions. The fine mesh region is a 80×80 square zone, with lower corner at grid point $(80, 80)$. Figure 5.1 shows the the numerical results. All three methods (the FDTD, GHC-FDTD, and GHF-FDTD algorithms) give correct solutions. The small square shows the boundary of the fine mesh region.

In the second test we test the stability for long time simulation. A random magnetic fields is given as the initial condition in the whole computational domain. We run the simulation for one million time steps in order to test the stability. Figure 5.2 shows the time history of the magnetic filed H_{zc} at a selected location in the computation domain by using two interpolation based subgridding methods. The computation for this model was performed using the coarse region

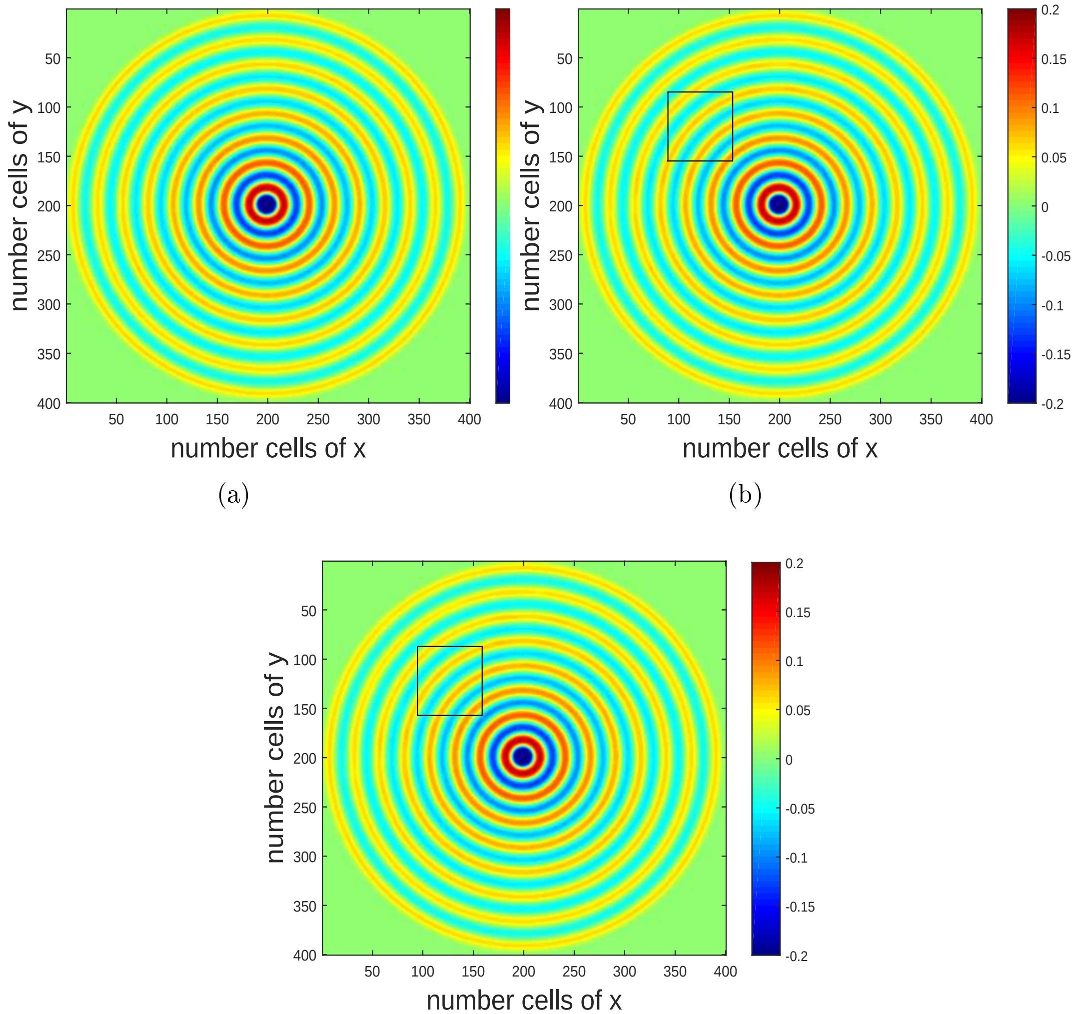

(a) (b) (c)

Figure 5.1: The magnetic field (H_{zc}) distribution using (a) the standard FDTD method; (b) the subgridding FDTD with ghost magnetic fields in the coarse region (GHC); and (c) the subgridding FDTD with ghost magnetic fields in the fine region (GHF). The square boxes indicates the boundary of the fine mesh region.

grid 200×200 cells and fine region grid 40×40 (a square zone with lower corner at grid point $(40, 40)$ to $(80, 80)$).

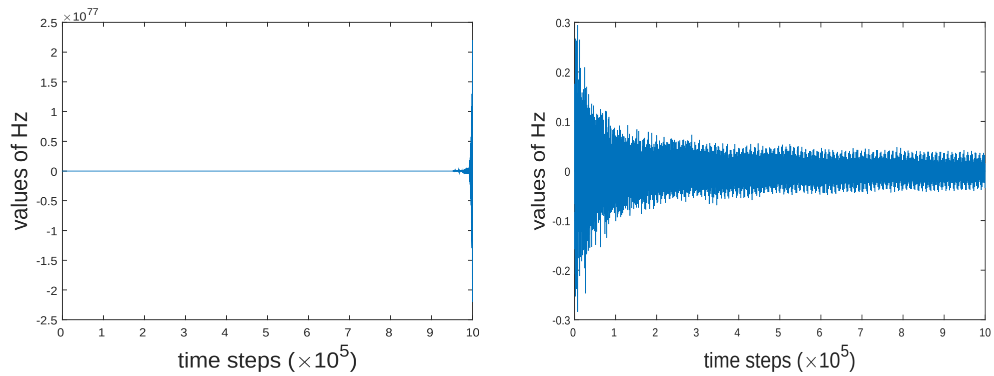

(a) (b)

Figure 5.2: Time history of the magnetic field (H_{zc}) using the (a) GHC, and (b) GHF methods for 1 million time steps.

As shown in Figure 5.2, the GHC method is unstable as the solution grows exponentially after about a few tens of thousand steps, while the GHF method is stable after one million steps.

In the next example, we apply the matrix stability analysis to a fully discrete problem on a finite domain with a single refinement patch. The stability of FDTD subgridding schemes can be studied by calculating the dominant eigenvalues of the amplification matrices [41, 54]. It states that the method is stable if all the eigenvalues of the update matrix lie inside or on the unit circle. In this test, the coarse region grid is 20×20 cells and the fine region contains 6×6 cells around the center of the domain. The maximum eigenvalues of the update matrix for different coarse region cells and different methods are shown in Table 5.1. Figure 5.3 and 5.4 show the distributions of the eigenvalues in complex plane for the GHC and GHF methods, respectively. For the GHC method, some eigenvalues locate outside of the unit circle and the largest eigenvalue shown in Table 5.1 is larger than 1, which indicating the late-time instability. The GHF method is stable as all eigenvalues lie on or inside the unit circle and the largest eigenvalue is 1 for all tested cases.

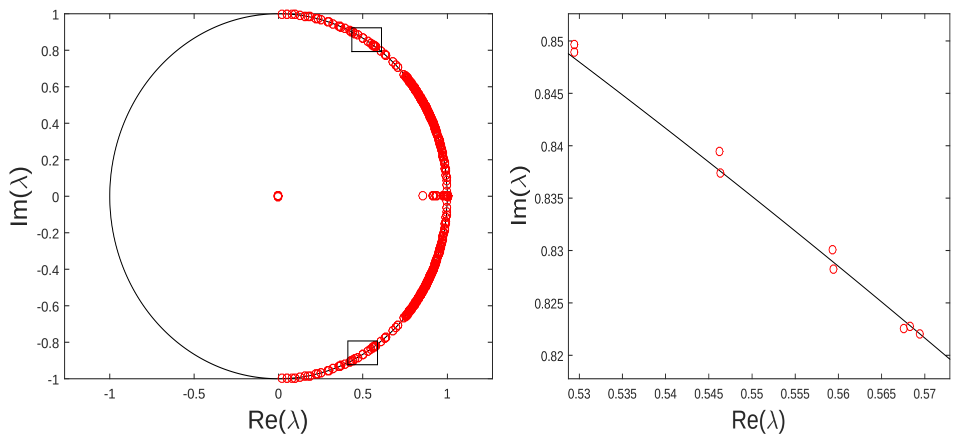

(a) (b)

Figure 5.3: (a) Distribution of the eigenvalues on the complex plane for the GHC method. (b) Zoom-in view of a region where some eigenvalues fall outside of the unit circle, $|\lambda| > 1$.

5.2 Numerical Examples for Temporal Subcycling Method

In this section, we assess the stability of the temporal subcycling FDTD algorithm by performing long time simulation and by eigenvalue test. The coarse and fine mesh ratio is 1:2, i.e., the time increment is Δt in the coarse grid region and $\Delta t/2$ in the fine mesh region. The incident source of a sine wave with wavelength $0.05\mu m$ is placed in the center of the domain. The computational grid size is 400×400. The fine mesh region is a 80×80 square zone, starting at grid point $(80, 80)$ to $(160, 160)$. The numerical results of the vacuum test is shown in Figure 5.5. The small square shows the boundary of the fine mesh region.

As shown in Figure 5.5, the numerical results of the vacuum test show that there are no significant reflection/scattering after the incident wave crosses the grid boundaries of coarse and fine meshes .

The convergent test is carried out for the proposed iteration based temporal subcycling method and the results are shown in Table 5.2. Solutions on very fine mesh is used as exact solution. As seen from the table, the rate of convergence of iteration based subcycling algorithm is second order.

Next, we assess the stability of the subcycling FDTD algorithm by eigenvalue test.

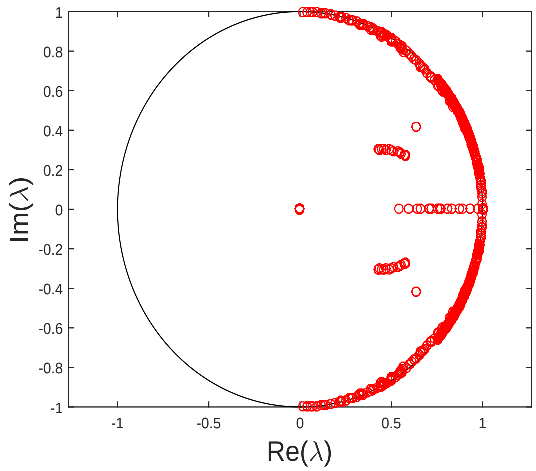

Figure 5.4: Distribution of the eigenvalues on the complex plane for the GHF method. All eigenvalues lie on or inside the unit circle.

Eigenvalues test results are shown in Figures 5.6, 5.7, Figure 5.8, and in Table 5.3. The result from Figures 5.7 shows that some eigenvalues locate outside of the unit circle with $|\lambda| > 1$, and Table 5.3 shows that the maximum eigenvalue for GE method is larger than 1. The GH and iteration based temporal subcycling methods have no eigenvalues outside the unit circle, and their largest eigenvalues are 1 for various grid sizes.

5.3 Numerical Examples for Iteration Based Subgrrding Algorithm

We combine the iteration based temporal subcycling and the spatial subgridding algorithm to obtain a subgridding method with both temporal and spatial refinement. We refer this method the iteration based subgridding (IBS) FDTD method. We performed several numerical tests in this section. The distance between the temporal fine region A and the spatial fine region B is 2 grid cells. The fine region B is inside the fine region A. The first numerical test is a vacuum test, and it is the same as the previous vacuum test with incident source at the center of the computational domain. The coarse mesh contains 400×400 cells, fine region A contains 84×84 cells, and the fine region B contains 80×80 cells. On the coarse grid and region A, $\Delta x = \Delta y = 0.002\mu m$. In the fine

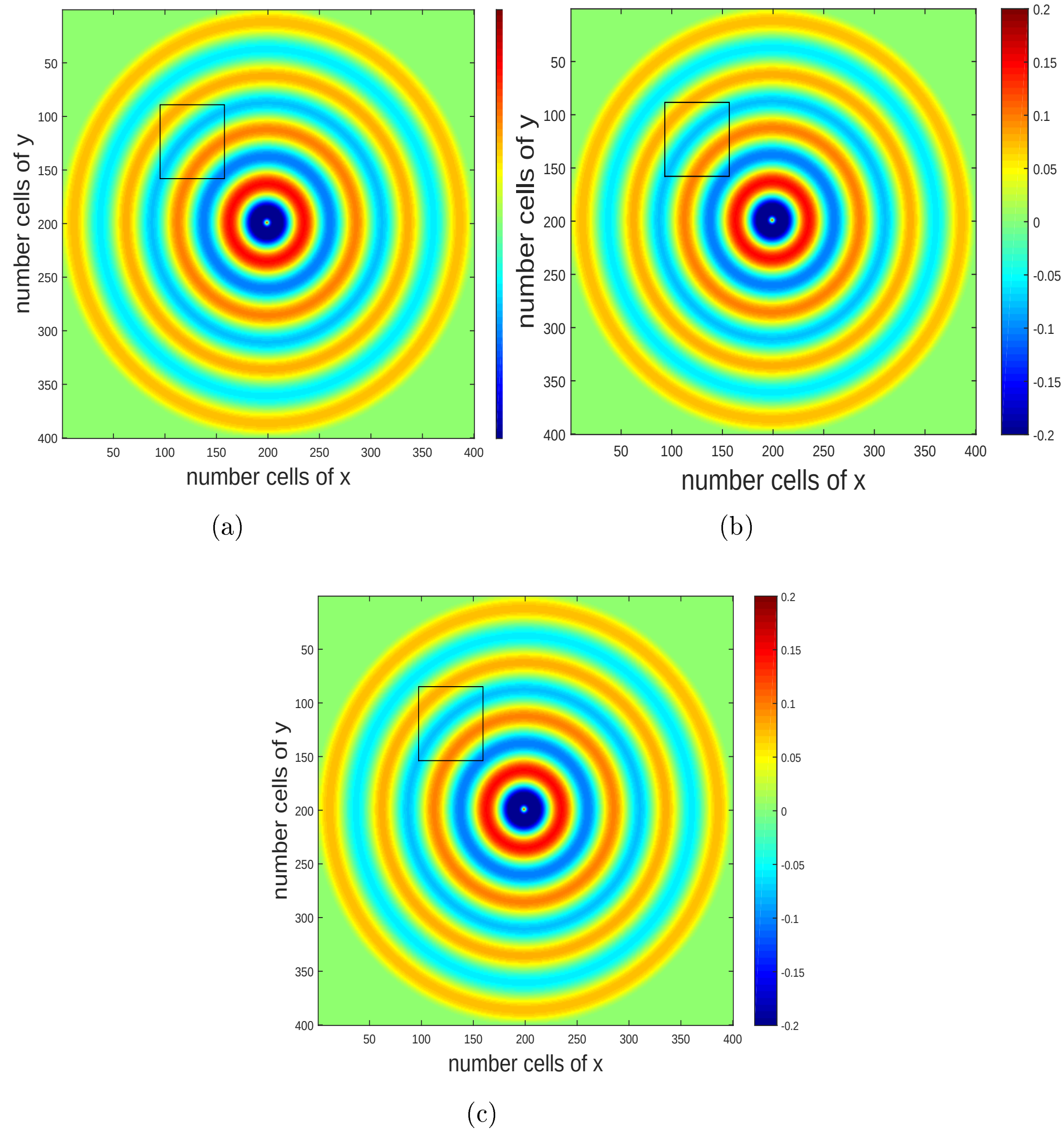

Figure 5.5: The figures show the magnetic field (H_{zc}) distribution using (a) the H ghost value (GH); (b) the E ghost value (GE); and (c) the iteration based temporal subcycling methods. The square box shows the boundary of the fine mesh region.

Spatial Subgridding algorithm	Mesh size	Maximum eigenvalue (round off error $\sim 10^{-14}$)
GHC	10×10	$1 + 1.97 \times 10^{-3}$
	20×20	$1 + 1.81 \times 10^{-3}$
	30×30	$1 + 1.15 \times 10^{-3}$
	40×40	$1 + 7.89 \times 10^{-4}$
GHF	10×10	$1 + 0.4 \times 10^{-14}$
	20×20	$1 + 0.6 \times 10^{-14}$
	30×30	$1 + 1.4 \times 10^{-14}$
	40×40	$1 + 1.8 \times 10^{-14}$

Table 5.1: List of the maximum eigenvalue for different coarse grid sizes and different subgridding methods.

Mesh size	L2-norm	order of convergence
10×10	2.84×10^{-2}	-
20×20	6.77×10^{-3}	2.07
40×40	1.68×10^{-3}	2.01
80×80	4.01×10^{-4}	2.07
160×160	8.68×10^{-5}	2.21

Table 5.2: Convergence test of the iteration based temporal subcycling FDTD algorithm.

region B the grid size is $\Delta x = \Delta y = 0.001\mu m$.

As shown in Figure 5.9, the numerical results of the vacuum test show good agreement between the IBS-FDTD method and the standard FDTD method.

Similar to the previous section, we test stability with random initial magnetic field for 1 million time steps. The computation for this model was performed using the coarse region grid 200×200 cells and 40×40 cells for fine region grid B. As shown in Figure 5.10, stable solution is obtained for the IBS-FDTD method after 1 million steps.

Figure 5.11 and Table 5.4 show the result of the eigenvalue test. Similar to the previous tests, the coarse region grid contains 20×20 cells and the fine region B grid contains 6×6 cells. Figure 5.11 shows that all the eigenvalues locate inside or on the unit circle with $|\lambda| \leq 1$. Table 5.4 confirms that the largest eigenvalue is 1 for all grid sizes, indicating the stability of the method.

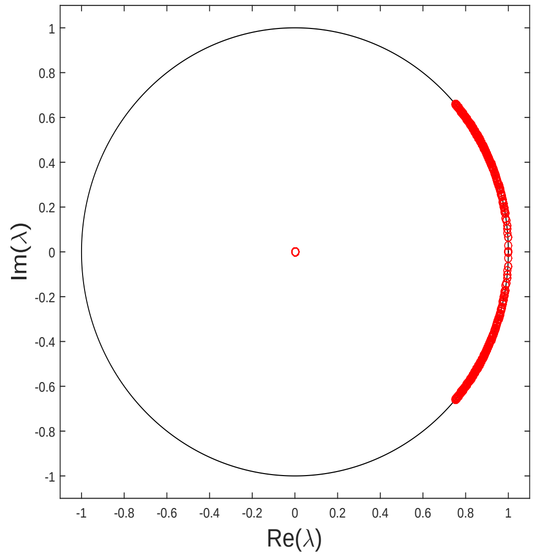

Figure 5.6: Distribution of the eigenvalues on the complex plane for the GH subgridding method. All eigenvalues lie on or inside the unit circle.

5.4 Numerical Simulations of Through-the-Wall Radar Imaging

In this section, we investigate through-the-wall radar imaging by using IBS FDTD method as forward problem solver and the imaging method in chapter 4. We set the room size to be $4m \times 4m$, and the object in the room be of varied sizes and shapes, with the material permittivity of the object to be $\epsilon_{obj} = 80$. In our test, we ignore the influence of wave propagation when cross the walls by setting the permittivity of the wall to be $\epsilon_w = 1$. The source is a Gaussian pulse with frequency $f = 600\ MHz$.

Figure 5.12 shows the ellipses constructed from a set of twelve transmitters and receivers around the room. There is a circular object in the room, the walls of the room is the square outlined in black, and the circular object is shown with a green outline. Ellipses from the reconstruction method are shown in red curves and the object is outlined in green. From Figure 5.12, we know that the ellipses surrounding the object, giving us information on where the object is. We separate Figure 5.12 into four figures (shown in Figure 5.13) that the ellipses constructed from a set of three transmitters and

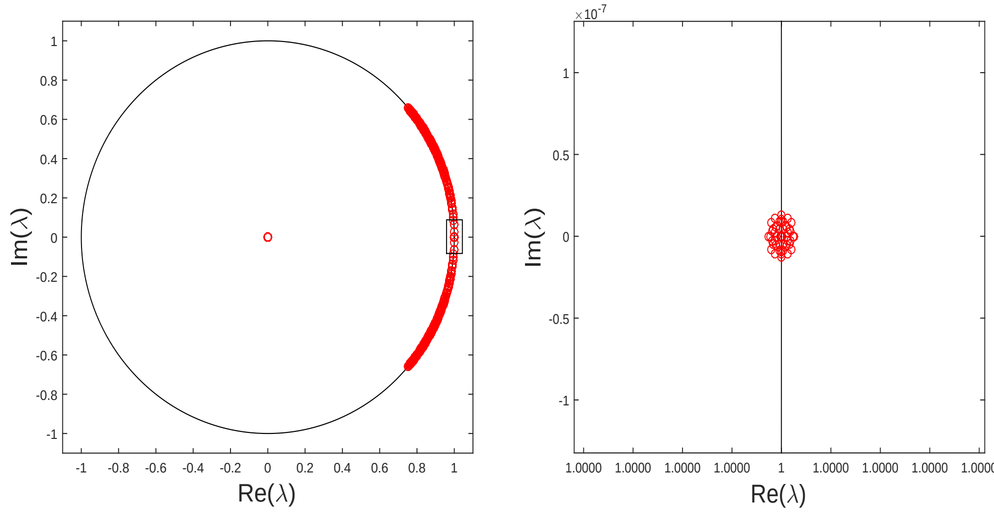

(a) (b)

Figure 5.7: (a) Distribution of the eigenvalues on the complex plane for the GE subgridding method. (b) Enlarged small region with some eigenvalues outside of the unit circle.

receivers on each side of the room. From Figure 5.13 we see that the object are externally tangent to these ellipses.

We compare the IBS-FDTD method with the standard FDTD method. Figure 5.14 shows the points on the boundary of the circular object from each method and the circular object. Figure 5.15 shows the points on the boundary of the square object from each method and the square object. The Table 5.5 shows the computational error of the results using the two methods with the actual object and computation times.

From the Table 5.5, we can find that the IBS method is more accuracy and efficiency than the standard FDTD method. We also try the reconstruction procedure of circular and squared objects with the location of the objects not in the center of the room. Also, we try two types of transmitters in each side of the room: one transmitter and multiple transmitters. We also try triangular objects. We only show the set of points on the boundary of the object found at the end of the iteration procedure and how closely they line up with the actual object being imaged.

As we can be seen from Figure 5.16 to Figure 5.21, the results with multiple (three) transmitters

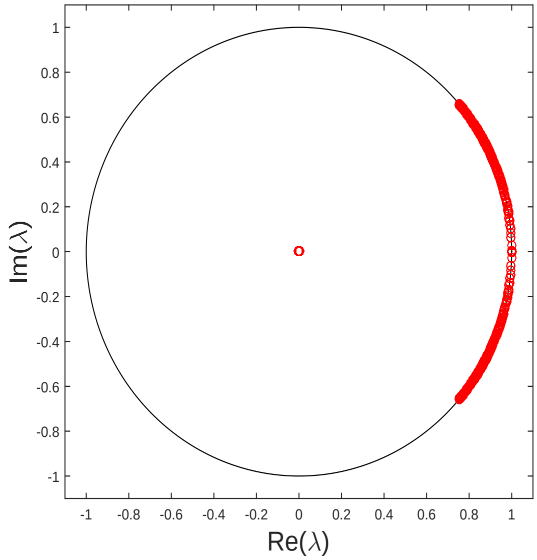

Figure 5.8: Distribution of the eigenvalues on the complex plane for the iteration based temporal subcycling method. All eigenvalues lie on or inside the unit circle.

on each side of the room are better than one transmitter. The circles, squares and rhombus are reconstructed fairly accurately. The triangular objects are the most challenging ones. This can be attributed to the sharp corners of the triangle. Figure 5.19 shows the final set of the points that are the tangency points of ellipses and the triangular object. We see that there has some "closet points" at the bottom of the triangle not on the boundary of the triangular object.

Temporal Subcycling Method	Mesh size	Maximum eigenvalue (round off error $\sim 10^{-14}$)
GH	10×10	$1 + 1.3 \times 10^{-14}$
	20×20	$1 + 1.6 \times 10^{-14}$
	30×30	$1 + 1.7 \times 10^{-14}$
	40×40	$1 + 3.2 \times 10^{-14}$
GE	10×10	$1 + 1.37 \times 10^{-8}$
	20×20	$1 + 1.29 \times 10^{-8}$
	30×30	$1 + 1.43 \times 10^{-8}$
	40×40	$1 + 1.28 \times 10^{-8}$
ITS	10×10	$1 + 0.9 \times 10^{-14}$
	20×20	$1 + 1.5 \times 10^{-14}$
	30×30	$1 + 1.9 \times 10^{-14}$
	40×40	$1 + 3.8 \times 10^{-14}$

Table 5.3: The max-eigenvalue for different coarse grid sizes and different temporal subcycling methods.

Mesh size	Maximum eigenvalue (round off error $\sim 10^{-14}$)
10×10	$1 + 0.4 \times 10^{-14}$
20×20	$1 + 0.8 \times 10^{-14}$
30×30	$1 + 2.0 \times 10^{-14}$
40×40	$1 + 2.3 \times 10^{-14}$

Table 5.4: List of the maximum eigenvalue for different grid sizes by using IBS FDTD method.

Actual object	Forward method	Mesh size	Computational error	CPU time
Circle diameter= $0.5m$	Standard FDTD	100×100	6.54%	13 seconds
	Standard FDTD	200×200	2.77%	326 seconds
	IBS-FDTD	100×100	2.79%	126 seconds
Square side= $0.5m$	Standard FDTD	100×100	10.89%	15 seconds
	Standard FDTD	200×200	5.94%	329 seconds
	IBS-FDTD	100×100	5.88%	124 seconds

Table 5.5: The computational error of the results using standard and IBS FDTD methods.

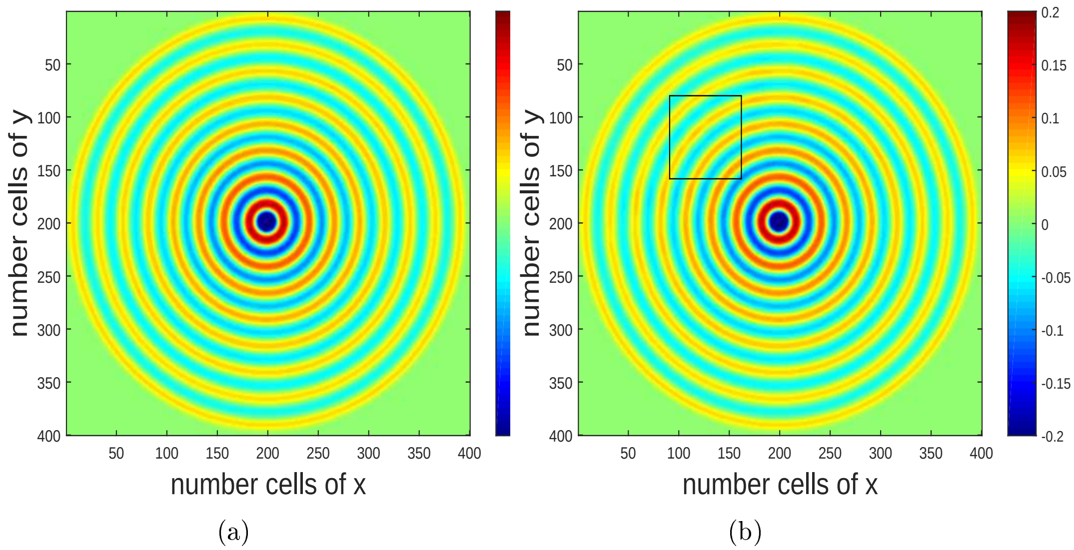

Figure 5.9: The magnetic field (H_{zc}) distribution using the (a) standard and (b) IBS FDTD methods. The square box is the boundary of fine region B.

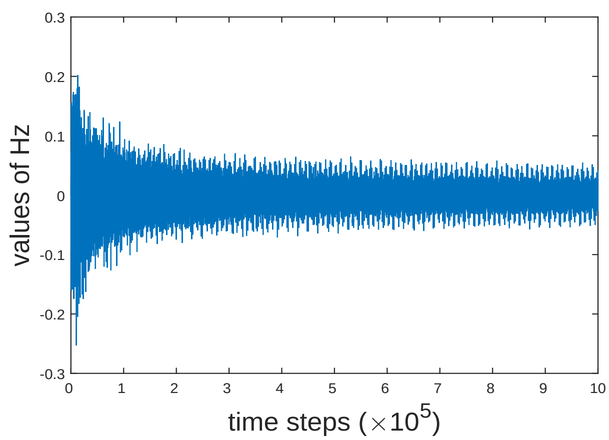

Figure 5.10: Time history of the magnetic field (H_{zc}) using the iteration based subgridding FDTD method for 1 million time steps.

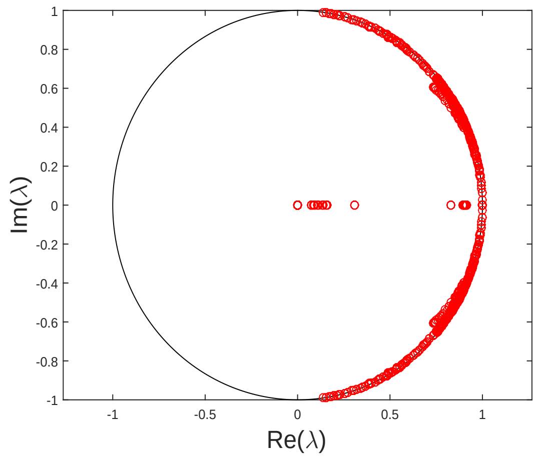

Figure 5.11: Distribution of the eigenvalues on the complex plane for the iteration based subgridding FDTD method.

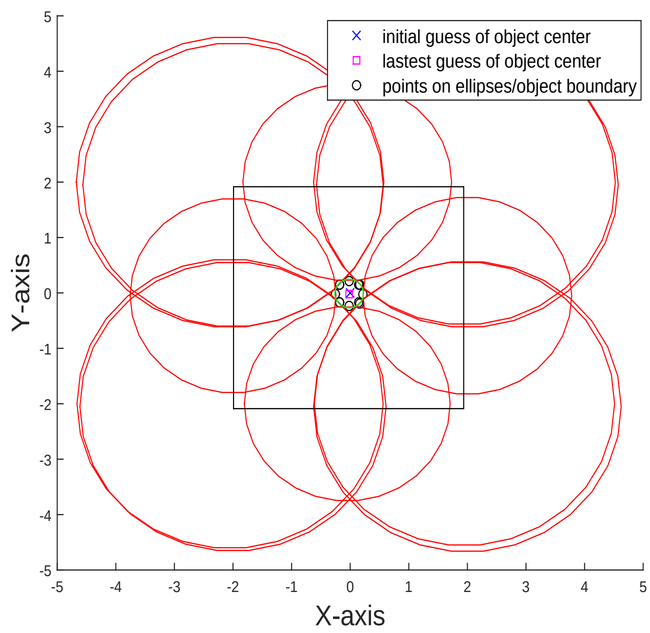

Figure 5.12: TWR object reconstruction. All of the ellipses constructed from the transmitters and receivers are shown in this figure. The set of ellipses encircles the object.

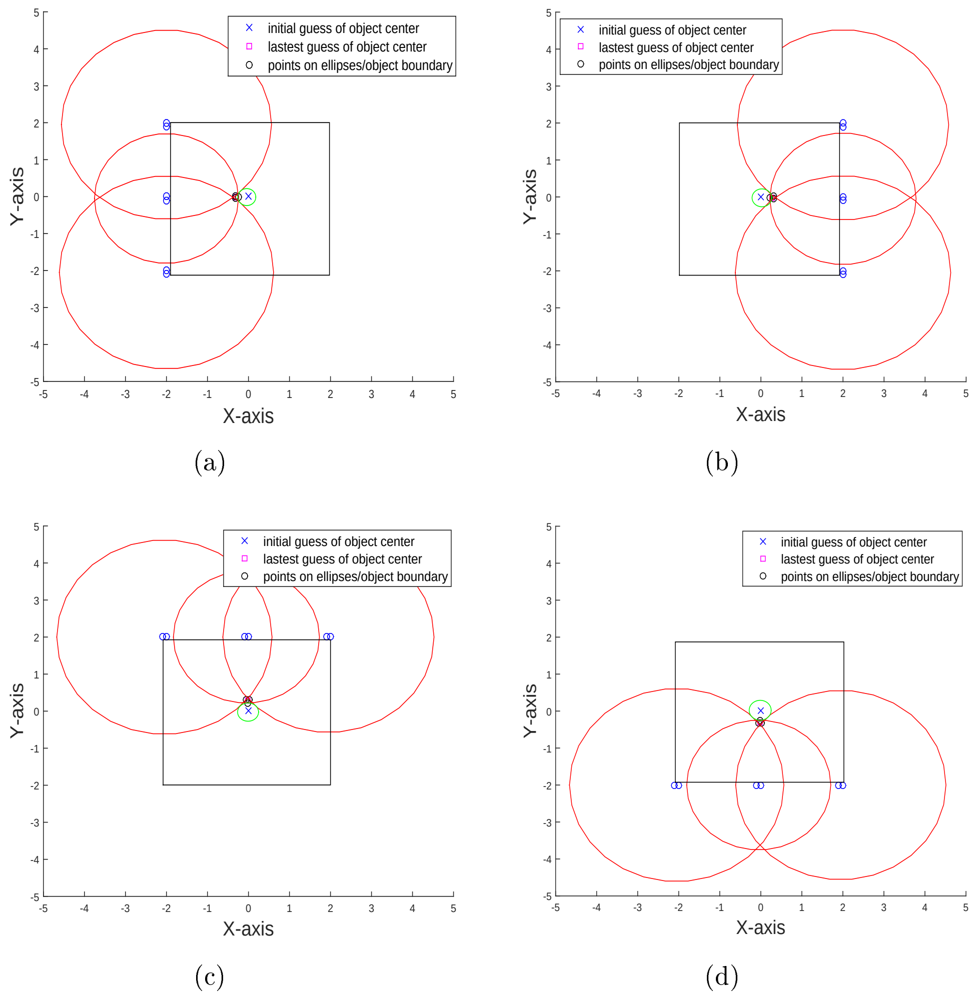

(a) (b) (c) (d)

Figure 5.13: Ellipses reconstructed from all of the transmitters and receivers on the (a) left, (b) right, (c) top, and (d) bottom sides. The square outlined in black is the walls of the room and the circle outlined in green is the circular object. The blue points in each images are the transmitters and receivers.

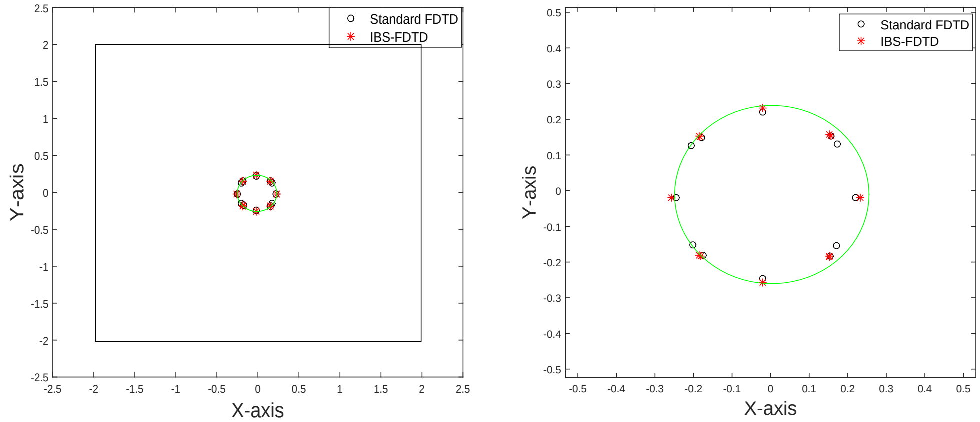

(a) (b)

Figure 5.14: Reconstructed circular objects using (a) the standard FDTD (black circle) and (b) the IBS-FDTD method (red circles). The square outlined in black color is the walls of the room and the circle outlined in green is the actual object. (b) enlarged image.

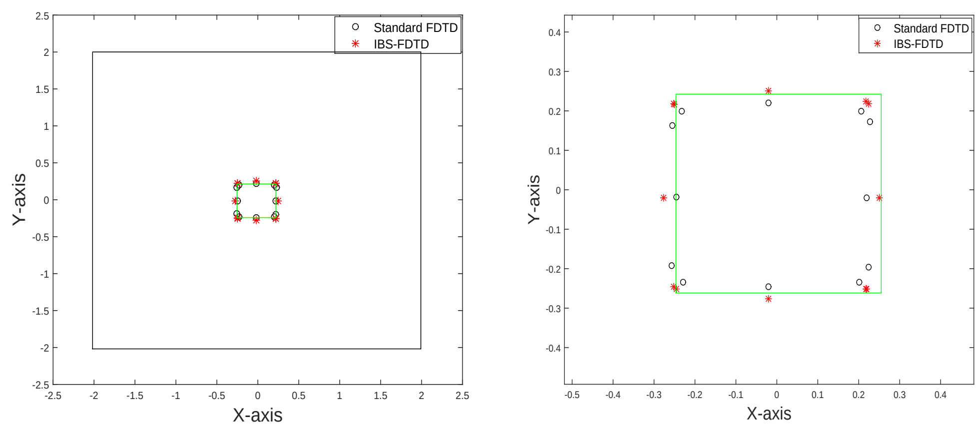

(a) (b)

Figure 5.15: Reconstructed squared objects using (a) the standard FDTD (black circle) and (b) the IBS-FDTD method (red circles). The square outlined in black color is the walls of the room and the object outlined in green is the actual object. (b) enlarged image.

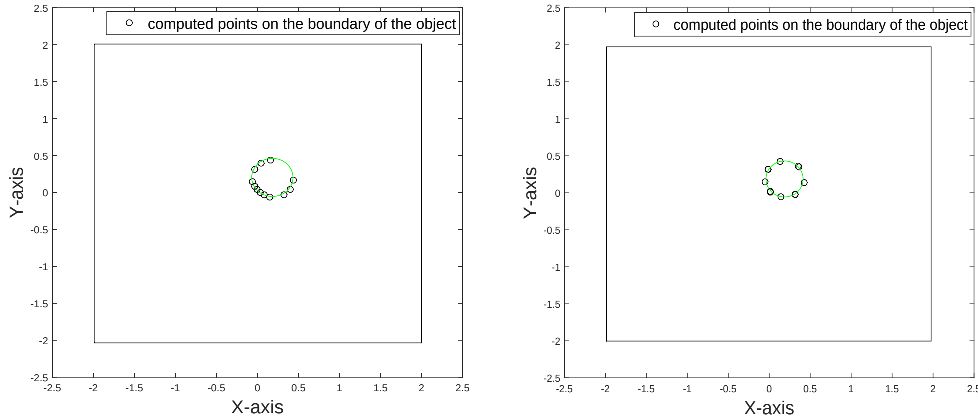

(a) (b)

Figure 5.16: Reconstruction of circular object (not centered at the room) using (a) one transmitter and (b) multiple transmitters. The square outlined in black is the walls of the room and the circle outlined in green is the actual circular object.

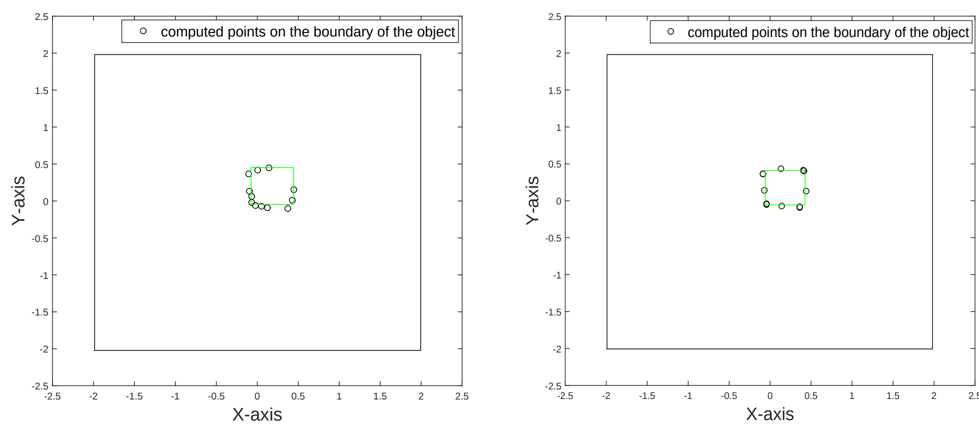

(a) (b)

Figure 5.17: Reconstruction of squared object (not centered at the room) using (a) one transmitter and (b) multiple transmitters. The square outlined in black is the walls of the room and the circle outlined in green is the actual squared object.

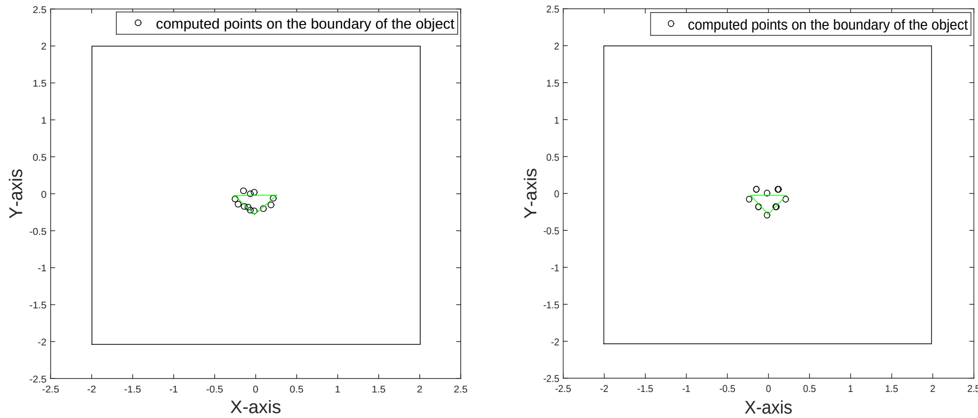

(a) (b)

Figure 5.18: Reconstruction of triangular object using (a) one transmitter and (b) multiple transmitters. The square outlined in black is the walls of the room and the triangular outlined in green is the actual triangular object.

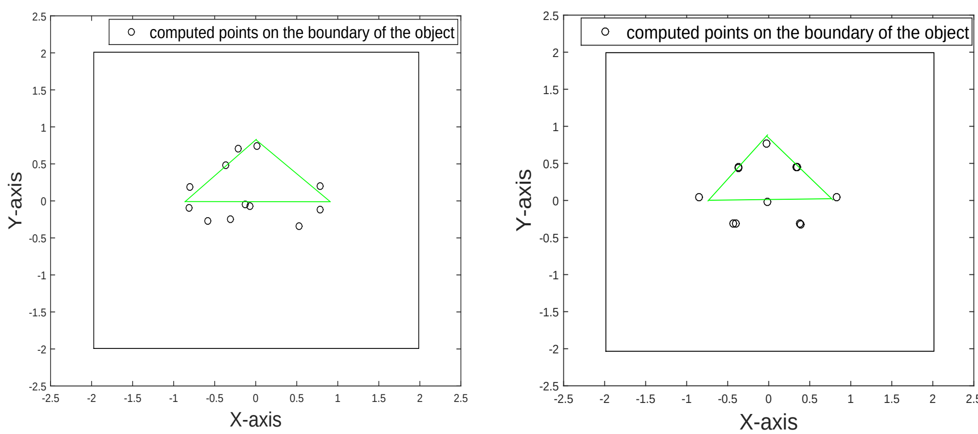

(a) (b)

Figure 5.19: Reconstruction of a larger triangular object using (a) one transmitter and (b) multiple transmitters. The square outlined in black is the walls of the room and the triangular outlined in green is the actual triangular object.

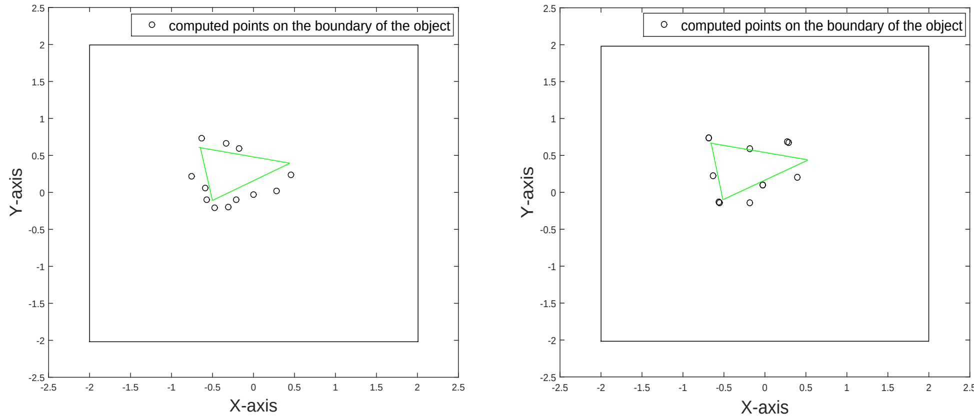

(a) (b)

Figure 5.20: Reconstruction of oblique triangular object (not centered at the room) using (a) one transmitter and (b) multiple transmitters. The square outlined in black is the walls of the room and the oblique triangular outlined in green is the actual oblique triangular object.

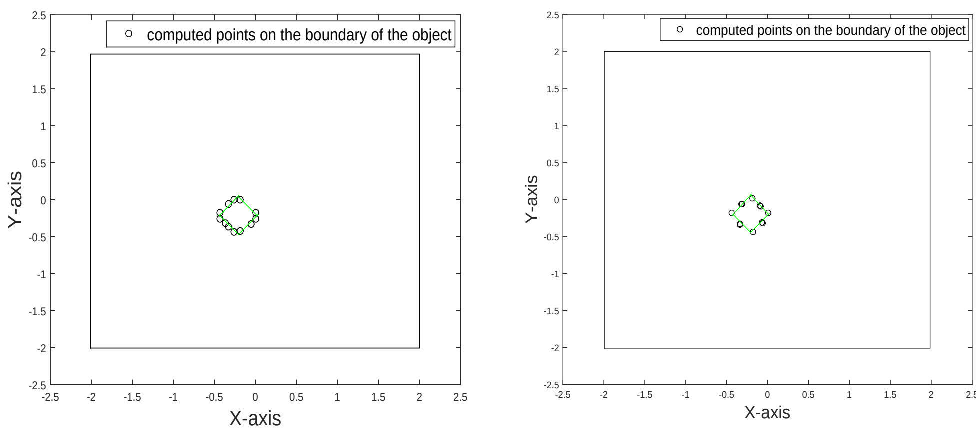

(a) (b)

Figure 5.21: Reconstruction of rhombus object (not centered at the room) using (a) one transmitter and (b) multiple transmitters. The square outlined in black is the walls of the room and the rhombus outlined in green is the actual rhombus object.

Chapter 6
CONCLUSIONS

In this dissertation we implement local temporal grid refinement (temporal subcycling) and spatial grid refinement (spatial subgridding) to the FDTD method for solving Maxwell's equations in two-dimensions. The refinement ratio is 2:1 in temporal and spatial domains, and the ghost value interpolation technique is applied to treat the coarse/fine mesh boundaries. We study the stability of the algorithm by eigenvalue tests and by performing simulations of large number of time steps. Differs from other subcycling/subgridding methods, our new method iterates the update equations near the temporal interface to obtain stable solutions. We use our method to solve the forward problem of electromagnetic scattering in the through-the-wall radar simulations, and then, we construct the inverse problem solution using the collected simulation data. Our results are consistent with the objects being analyzed. Also, the results show that our method is more accurate and efficient than the standard FDTD method.

For the further work, we will extend our method to three dimensions. We will also consider to study the object reconstruction algorithm for multiple objects for TWR system.

REFERENCES

[1] I. Ahmed, Z. Chen. A hybrid ADI-FDTD subgridding scheme for efficient electromagnetic computation. *Int. J. Numer. Model.*, 17:237-249, 2004.

[2] J. P. Berenger. A perfectly matched layer for the absorption of electromagnetic waves. *J. Comput. Phys.*, 114:185-200, 1994.

[3] J. P. Berenger. The Huygens subgridding for the numerical solution of the Maxwell equations. *J. Comput. Phys.*, 230:5635-5659, 2011.

[4] T. Bergmann, J. O. A. Robertsson, K. Holliger. Finite-difference modelling of electromagnetic wave propagation in dispersive and attenuating media. *Geophysics*, 63:856-867, 1998.

[5] R. Biedron, J. Thomas. A generalized patched-grid algorithm with application to the F-18 forebody with actuated control strake. *Computing Systems in Engineering.*, 1(2-4):563-576, 1990.

[6] J. M. Bourgeois, G. S. Smith. A fully three-dimensional simulation of a ground-penetrating-radar: FDTD theory compared with experiment. *IEEE Transactions on Geoscience and Remote Sensnsing*, 34:36-44, 1996.

[7] A. Bugaev, V. Chapursky, S. Ivashov, V. Razevig, A. Sheyko, I. Vasilyev. Through wall sensing of human breathing and heart beating by monochromatic radar. *Proceedings of the Tenth International Conference on Ground Penetrating Radar*, 1:291-294, 2004.

[8] Richard L. Burden, J. Douglas Faires. Numerical Analysis. *PWS, 3rd edition*, 1985.

[9] N. Cassidy. The application of mathematical modelling in the interpretation of ground penetrating radar data. *PhD Thesis, Keele University, UK*, 2001.

[10] A. Chandra, D. Gaikwad, D. Singh, M. Nigam. An approach to remove the clutter and detect the target for ultra-wideband through-wall imaging. *J. Geophys. Eng.*, 5(4):412-419, 2008.

[11] Matthew Charnley, Aihua Wood. Through-the-wall radar detection analysis via numerical modeling of Maxwell's equations. *J. Comput. Phys.*, 313:532-548, 2016.

[12] M.W. Chevalier, R.J. Luebbers. FDTD local grid with material traverse. *IEEE Trans. Antennas Propag.*, 45:411-421, 1997.

[13] F. Collino, T. Fouquet, P. Joly. A space-time mesh refinement method for the 1D Maxwell's equation. *C. R. Acad. Sci. Paris*, 328:263-268, 1999.

[14] F. Collino, T. Fouquet, P. Joly. Conservative space-time mesh refinement methods for the FDTD solution of Maxwell's equations,. *J. Comput. Phys.*, 211:9-35, 2006.

[15] J. Crank, P. Nicolson. A practical method for numerical evaluation of solutions of partial differential equations of the heat conduction type. *Proc. Camb. Phil. Soc.*, 43:50-67, 1947.

[16] D.J. Daniels. Ground Penetrating Radar. *Institution of Engineering and Technology, 2nd edition*, 2004.

[17] G. Franceschetti, R. Lanari. Synthetic Aperture Radar Processing. *CRC Press*, 1999.

[18] A. Giannopoulos. The investigation of transmission-line matrix and finite-difference time-domain methods for the forward problem of ground probing radar. *University of York, UK*, 1997.

[19] A. Giannopoulos. Modelling of ground penetrating radar using GprMax. *Construction and Building Materials*, 19:755-762, 2005.

[20] A. C. Gurbuz, J. H. McClellan, W. R. Scott. Compressive sensing for subsurface imaging using ground penetrating radar. *Signal Processing*, 89:1959-1972, 2009.

[21] B. Gustafsson, H. O. Kreiss, Sundström. Stability theory of difference approximations for mixed initial boundary value problems II. *Math. Comp.*, 26:649-686, 1972.

[22] B. Gustafsson, H. O. Kreiss, J. Oliger. Time Dependent Problems and Difference Methods. *New York, Wiley*, 1995.

[23] J. D. Jackson. Classical Electrodynamics. *Wiley, New York, 2nd edition*, 1962.

[24] I.S. Kim, W.J. Hoeffer. A local mesh refinement algorithm for the time-domain finite-difference method using Maxwell's curl equations. *IEEE Trans. Microw. Theory Tech.*, 38:812-815, 1990.

[25] E. Lagunas, M. G. Amin, F. Ahmad, M. Najar. Joint wall mitigation and compressiev sensing for indoor image reconstruction. *IEEE Transactions on Geoscience and Remote Sensing*, 51(2):891-905, 2013.

[26] K. J. Langenberg, M. Brandfass, K. Mayer, T. Kreutter, A. Brull, P. Felinger, D. Huo. Principles of microwave imaging and inverse scattering. *EARSeL Adv. Remote Sens*, 2, 1993.

[27] Jing Li, Fengshan Liu, Penglong Xu, Zhaofa Zeng, G. Charmaine Gilbreath, Chadwick Todd Hawley. Simulation and signal processing of through wall UWB radar for human being's periodic motions detection. *Proc. SPIE*, 8734, 2013.

[28] J. Liu, M. Brio, J. V. Moloney. Transformation optics based local mesh refinement for solving Maxwell's equations. *J. Comput. Phys.*, 258:359-370, 2014.

[29] P. Monk. Sub-gridding FDTD schemes. *ASES Journal*, 11:37-46, 1996.

[30] R.M. Narayanan, M.C. Shastry, P.H. Chen, M. Levi. Through-the-wall detection of stationary human targets using Doppler radar. *Prog. Electromagn. Res.*, 20:147-166, 2010.

[31] R. G. Newton. Scattering Theory of Waves and Particles. *Dover*, 2002.

[32] M. Okoniewski, E. Okoniewska, M. A. Stuchly. Three dimensional subgridding algorithm for FDTD. *IEEE Trans. Antennas Propag.*, 45:422-429, 1997.

[33] J. E. Peabody, G. L. Charvat, J. Goodwin, M. Tobias. Through-wall imaging radar. *Lincoln Laboratory Joural*, 19(1), 2012.

[34] D. T. Prescott, N. V. Shuley. A method for incorporating different sized cells into the finite-difference time-domain analysis technique. *IEEE Microw. Guided Wave Lett.*, 2:434-436, 1992.

[35] Shobha Sundar Ram, Yang Li, Adrian Lin, Hao Ling. Doppler-based detection and tracking of humans in indoor environments. *J. Franklin Inst.*, 345:679-699, 2008.

[36] R. F. Remis. On the stability of the finite-difference time-domain method. *J. Comput. Phys.*, 163:249-261, 2000.

[37] D. T. Shimizu, M. Okoniewski, M. A. Stuchly. An efficient subgriding algorithm for FDTD. *Progress Appl. Computat. Electromagn.*, 762-766, 1995.

[38] E. M. Staderini. UWB radar in medicine. *IEEE Aerospace and Electronic Systems Magazine*, 17(1), 2002.

[39] I. Stakgold. Greens Functions and Boundary Value Problem. *Wiley-Interscience, 2nd edition*, 1997.

[40] A. Taflove, M. E. Brodwin. Numerical Solution of Steady-State Electromagnetic Scattering Problems Using the Time-Dependent Maxwell'S Equations. *IEEE Trans. Microwave Theory Tech.*, 23:623-630, 1975.

[41] A. Taflove, S. Hagness. Computational Electrodynamics: The Finite-Difference Time-Domain Method. *Artech House, Norwood, MA, 3rd edition*, 2005.

[42] Fernando L. Teixeira. Time-Domain finite-difference and finite-element methods for Maxwell equations in complex media. *IEEE Trans. Antennas Propag.*, 56:2150-2166, 2008.

[43] P. Thoma, T. Weiland. A consistent subgridding scheme for the finite difference time domain method. *Int. J. Numer. Anal. Mod.*, 9:359-374, 1996.

[44] L. N. Trefethen. Group velocity interpretation of the stability theory of Gustafsson, Kreiss and Sundström. *J. Comput. Phys.*, 49:199-217, 1983.

[45] L. N. Trefethen. Instability of difference models for hyperbolic initialboundary value problems. *Comm. Pure and Appl. Math.*, 37:329-367, 1984.

[46] L. N. Trefethen. Stability of finite difference models containing two boundaries or interfaces. *Comm. Pure and Appl. Math.*, 37:329-367, 1984.

[47] F. Treves. Basic Linear Partial Differential Equations. *Academic*, 1975.

[48] A. Vaccari, R. Pontalti, C. Malacarne, L. Cristoforetti. A robust and efficient subgridding algorithm for finite-difference time-domain simulations of Maxwell's equations. *J. Comput. Phys.*, 194:117-139, 2004.

[49] S. Wang, F. L. Teixeira, R. Lee, J. F. Lee. Optimization of subgridding schemes for FDTD. *IEEE Microw.Wireless Comp. Lett.*, 12:223-225, 2002.

[50] K. Xiao, D. J. Pommerenke, J. L. Drewniak. A three-dimensional FDTD subgridding algorithm with separated temporal and spatial interfaces and related stability analysis. *IEEE TAP*, 55:1981-1990, 2007.

[51] K. S. Yee. Numerical Solution Of Initial Boundary Value Problems Involving Maxwell'S Equations in Isotropic Media. *IEEE Trans. Antennas Propag.*, 14:302-307, 1966.

[52] W. Yu, R. Mittra. A new subgridding method for the finite-difference time-domain algorithm. *IEEE Microw. Opt. Technol. Lett.*, 21:330-333, 1999.

[53] A. R. Zakharian, M. Brio, J. V. Moloney. FDTD based local mesh refinement method for Maxwell's equations in two space dimensions. *Commun. Math Sci.*, 2:497-513, 2004.

[54] A. R. Zakharian, M. Brio, C. Dineen, J. V. Moloney. Stability of 2D FDTD Algorithms with Local Mesh Refinement for Maxwell's Equations. *Commun. Math Sci.*, 4:345-374, 2006.

[55] S. S. Zivanovic, K. S. Yee, K. K. Mei A subgriding method for the time-domain finite-difference method to solve Maxwell's equations. *IEEE Trans. Microwave Theory Tech.*, 39:471-479, 1991.